Tri-component-pairing chiral superconductivity on the honeycomb lattice with mixed *s*- and *d*-wave symmetries

Yu-Hang Li,[1] Jiarui Jiao,[1] Xiao-Xiao Zhang,[2] Congjun Wu,[3,4,5,6,*] and Wang Yang[1,†]

[1]*School of Physics, Nankai University, Tianjin 300071, China*

[2]*Wuhan National High Magnetic Field Center and School of Physics, Huazhong University of Science and Technology, Wuhan 430074, China*

[3]*New Cornerstone Science Laboratory, Department of Physics, School of Science, Westlake University, Hangzhou 310024, Zhejiang, China*

[4]*Institute for Theoretical Sciences, Westlake University, Hangzhou 310024, Zhejiang, China*

[5]*Key Laboratory for Quantum Materials of Zhejiang Province, School of Science, Westlake University, Hangzhou 310024, Zhejiang, China*

[6]*Institute of Natural Sciences, Westlake Institute for Advanced Study, Hangzhou 310024, Zhejiang, China*

(Received 26 April 2025; revised 22 October 2025; accepted 17 December 2025; published 9 January 2026)

In this work, we investigate chiral topological superconductors on a two-dimensional honeycomb lattice with coexisting $d_{x^2-y^2}$, d_{xy}, and s-wave pairing symmetries. Using a Ginzburg-Landau free energy analysis, the pairing gap function is shown to exhibit a tri-component form $s + d_{x^2-y^2}e^{i\phi_1} + d_{xy}e^{i\phi_2}$, where ϕ_1 and ϕ_2 are phase differences between the d- and s-wave pairing components, which spontaneously breaks both time reversal and C_6 rotational symmetries. Chern numbers of the energy bands are calculated to be nonzero, demonstrating the topologically nontrivial nature of the system. The anomalous AC Hall conductivity is computed, which is not invariant under C_6 rotations, reflecting the anisotropic nature of the pairing gap function. Fractional magnetic vortices are also discussed, arising from the multicomponent nature of the pairing gap function.

DOI: 10.1103/954n-3cch

I. INTRODUCTION

Chiral superconductors [1] have attracted intense research interests because of their potentials in realizing topological quantum computations [2–18]. Typical chiral pairing states include chiral p-wave [19–27], d-wave [28–32], and f-wave pairings [33–37], corresponding to orbital angular momentum of a Cooper pair equal to one, two, and three, respectively. Possible chiral d-wave superconductors include certain copper-oxide high-temperature superconductors [38–42] and honeycomb correlated systems [43–45]. Based on the doped Hubbard model on the honeycomb lattice, it is theoretically proposed that superconductivity arising from correlated electrons may take the form of a chiral $d \pm id$ singlet pairing or a $p \pm ip$ triplet pairing, depending on the doping level and interaction strength [46–49]. At doping levels near the van Hove singularity (VHS), the $d \pm id$ singlet pairing dominates at weak coupling, while the $p \pm ip$ triplet pairing becomes more prominent when the interaction strength increases [50]. Recently, there has been evidence that the surface of YPtBi material may host chiral $d + id$ superconducting pairing [51,52].

Exotic chiral superconductivities can also emerge from multilayer systems. For example, recent studies have revealed the possible presence of chiral d-wave superconducting pairing in twisted bilayer graphene [53–62]. Interestingly, it has been proposed in Ref. [32] that the method of twisting bilayer materials provides a strategy to stack two layers of Bi2212 thin films together and rotate them at a certain angle. When the twist angle increases from 0° to 45° in the twisted cuprate system, the pairing symmetry transitions from $s \pm id$ to $d_{x^2-y^2} \pm id_{xy}$ [32,63,64]. In addition, the study of a superconducting heterojunction with one side characterized by the $p_x \pm ip_y$ gap function and the other side the conventional s-wave one found the pairing pattern to be $s + i\eta_1[e^{i\eta_2\phi/2}p_x + \eta_3 e^{-i\eta_2\phi/2}p_y]$ with $\eta_j = \pm 1 (j = 1, 2, 3)$, where ϕ is the phase difference between the p_x- and p_y-wave pairing components [65].

One significant feature of chiral superconductivity is the spontaneous breaking of time reversal symmetry, as signified by the non-collinear phase difference between different components of pairing order parameters. Time-reversal symmetry breaking can be detected through various methods, such as muon spin relaxation experiments [66,67], Josephson interference measurements [68–73], the magneto-optical Faraday effect [74], and Kerr rotation experiments [75–79]. In Kerr rotation experiments, the system breaking time-reversal symmetry typically exhibits a nonzero Kerr rotation angle of light, meaning that the polarization direction of reflected light rotates. This effect can be measured using ultrahigh sensitivity zero-field Kerr effect measurements. Since the Kerr angle is related to the AC Hall conductivity σ_H under zero external magnetic field, a nonvanishing AC Hall conductivity is an evidence for the existence of time reversal symmetry breaking in the system [80,81].

In this paper, we investigate chiral superconductors on a honeycomb lattice in the case where nearest-neighbor pairing dominates, with coexisting $d_{x^2-y^2}$, d_{xy}, and s-wave pairing symmetries. The coexistence of these three pairing symmetries can be either intrinsic or extrinsic, where "intrinsic" refers to simultaneous instabilities in the three superconducting channels in the material, and "extrinsic" refers to the situation where the coexistence is induced via the proximity

*Contact author: wucongjun@westlake.edu.cn

†Contact author: wyang@nankai.edu.cn

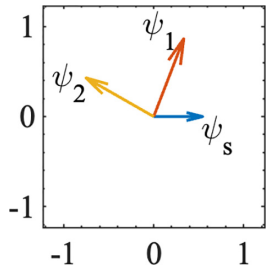

FIG. 1. One of the twelve degenerate configurations of the tri-component-pairing gap function on a honeycomb lattice, in which ψ_s, ψ_1, and ψ_2 represent the s-, $d_{x^2-y^2}$-, and d_{xy}-pairing components, respectively. The phase of s-wave order parameter is fixed to zero, i.e., $|\psi_s| + |\psi_1|e^{i\phi_1} + |\psi_2|e^{i\phi_2}$. The choices of the values of parameters in the free energy are included in the text. It is worth emphasizing that the two components ψ_1 and ψ_2 in the figure have a phase difference of 0.452π, not perpendicular with each other.

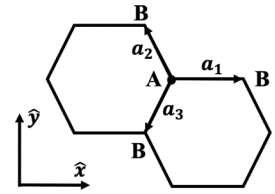

FIG. 2. Schematic plot of a two-dimensional honeycomb lattice, where A and B denote sites in the two inequivalent sublattices. The three nearest-neighbor vectors for the sublattice site A are shown as the black arrows as $\boldsymbol{a_1} = (a, 0)$, $\boldsymbol{a_2} = (-a/2, \sqrt{3}a/2)$, and $\boldsymbol{a_3} = (-a/2, -\sqrt{3}a/2)$, in which the lattice constant of the honeycomb lattice is a. The x direction is taken as the direction pointing from sublattice site A to B, and the y direction is in the perpendicular direction.

effect by superimposing a conventional s-wave superconductor on top of a chiral $d \pm id$ one. The experimentally observed nematic superconductivity in twisted bilayer graphene [61] has been proposed to be possibly arising from the intrinsic coexistence of these pairing components as discussed in Ref. [62]; while the extrinsic scenario is applicable to any $d + id$ pairing material in proximity with an s-wave one. As to be discussed shortly, the C_6 rotational symmetry is spontaneously broken for the tri-component-pairing, whereas the $d \pm id$ pairing preserves this symmetry. Hence, the resulting anisotropic Hall response signals can serve as signatures for nematic superconductivity in the "intrinsic" case, and chiral $d \pm id$ pairing in the "extrinsic" case in the materials.

From a free energy perspective, there are complex frustrations and intertwinings among the $d_{x^2-y^2}$-, d_{xy}-, and s-wave pairing components. On the one hand, the quadratic Josephson couplings favor a relative $\pm\pi/2$ phase difference between any two of the three pairing symmetries; and on the other hand, the existence of an exotic quartic term in the free energy which is first order in ψ_s and cubic in d-wave components favors a phase difference of $n\pi$ (or $m\pi/2$) between the $d_{x^2-y^2}$- (or d_{xy}-) wave and s-wave pairings, where both m and n are integers. However, the phase differences among the three pairing components cannot simultaneously satisfy all these conditions. Based on a Ginzburg-Landau (GL) free energy analysis, we find that the pairing gap function is of the form $s + d_{x^2-y^2}e^{i\phi_1} + d_{xy}e^{i\phi_2}$, where ϕ_1 (and ϕ_2) represents the phase difference between the $d_{x^2-y^2}$- (and d_{xy}-) wave and the s-wave pairing order parameters as shown in Fig. 1.

The obtained pattern of tri-component-pairing $s + d_{x^2-y^2}e^{i\phi_1} + d_{xy}e^{i\phi_2}$ not only spontaneously breaks the time-reversal symmetry, but also breaks the spatial C_{6v} symmetry of the honeycomb lattice down to C_2. The breaking of time reversal symmetry manifests itself in the nonvanishing Hall conductivity, whereas the absence of C_6 rotational symmetry in the pairing gap function can be detected through the spatial anisotropy in Hall conductivity and Kerr effect. Furthermore, we have confirmed that the pairing is topologically nontrivial by showing the nonvanishing of the Chern number and the emergence of a Majorana edge mode on the boundaries.

Because of the multicomponent structure of the pairing gap function, the system can host exotic topological excitations, not possible in superconductors with a single pairing component. In particular, we show in detail that the tri-component-pairing superconductivity can host magnetic vortices carrying arbitrary fractions of the magnetic flux quantum [82]. Other exotic topological excitations such as chiral skyrmions can also exist in the tri-component-pairing system [83]. Three-component superconductors have been studied to some extent, revealing spontaneous time-reversal symmetry breaking [84], and novel topological solitons [85].

The rest of the paper is organized as follows. In Sec. II, we begin with a GL free energy analysis, from which the form of the pairing gap function and the symmetry breaking pattern are derived. In Sec. III, by using a microscopic Bogoliubov-de Gennes (BdG) Hamiltonian of a pairing gap function $s + d_{x^2-y^2}e^{i\phi_1} + d_{xy}e^{i\phi_2}$ on the honeycomb lattice, we show the opening of the topological mass gap and the nonzero Chern number. The anisotropic anomalous AC Hall conductivity is studied in Sec. IV. In Sec. V, fractional magnetic vortices are discussed. Conclusions are presented in Sec. VI.

II. GINZBURG-LANDAU FREE ENERGY ANALYSIS

A. Uniform Ginzburg-Landau free energy

We consider a superconducting system on the honeycomb lattice as shown in Fig. 2. The superconducting pairing gap function will be shown to exhibit a tri-component form with competing $d_{x^2-y^2}$-, d_{xy}-, and s-wave pairing symmetries, based on a combination of symmetry and GL free energy analysis.

The point group symmetry of a monolayer of honeycomb lattice is C_{6v}, which contains six rotations and six reflections, as shown in Fig. 3. The most general GL free energy respecting the U(1) gauge, the time reversal, and the C_{6v} point group symmetries up to the quartic order is given by:

$$F = F_s^{(0)} + F_d^{(0)} + F^{(4)}, \tag{1}$$

in which

$$\begin{aligned} F_s^{(0)} &= \alpha_s|\psi_s|^2 + \beta_s|\psi_s|^4, \\ F_d^{(0)} &= \alpha_d(|\psi_1|^2 + |\psi_2|^2) + \beta_d(|\psi_1|^2 + |\psi_2|^2)^2, \end{aligned} \tag{2}$$

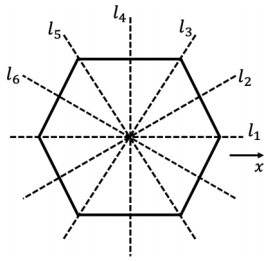

FIG. 3. Schematic plot of the twelve symmetry elements of the C_{6v} group consisting of six rotation and six reflection operations. The rotation operations are represented as C_6, C_3, C_2, C_3^2 and C_6^5 in the text, corresponding to rotations around z axis by angles $\pi/3$, $2\pi/3$, π, $4\pi/3$, and $5\pi/3$. The six reflection planes of the reflection operations are determined by the planes spanned by z axis and the dashed lines l_1, l_2, l_3, l_4, l_5, l_6.

and

$$\begin{aligned} F^{(4)} = {} & \gamma|\psi_s|^2(|\psi_1|^2+|\psi_2|^2) + g_{dd}(\psi_1^*\psi_2 - \psi_1\psi_2^*)^2 \\ & + g_{sd}\left[\psi_s^{*2}\left(\psi_1^2+\psi_2^2\right) + \psi_s^2\left(\psi_1^{*2}+\psi_2^{*2}\right)\right] \\ & + g'_{sd}[(\psi_s^*\psi_1 + \psi_s\psi_1^*)(|\psi_1|^2 - |\psi_2|^2) \\ & - (\psi_s^*\psi_2 + \psi_s\psi_2^*)(\psi_1^*\psi_2 + \psi_1\psi_2^*)], \end{aligned} \tag{3}$$

where ψ_s, ψ_1 and ψ_2 represent the complex order parameters for the s-wave, $d_{x^2-y^2}$-wave, and d_{xy}-wave, respectively; $\alpha_s < 0$, $\alpha_d < 0$, $\beta_s > 0$, $\beta_d > 0$ in the superconducting phase when three pairing symmetries coexist; γ represents the phase-independent coupling term between the s-wave and d-wave pairing components; $g_{dd} > 0$ is the coefficient of the term which contains the quadratic Josephson coupling $\psi_1^2\psi_2^{*2} + h.c.$ between $d_{x^2-y^2}$- and d_{xy}-wave components; $g_{sd} > 0$ is the coefficients of the quadratic Josephson coupling $\psi_s^{*2}(\psi_1^2 + \psi_2^2) + \text{H.c.}$ between s- and d-wave components; g'_{sd} represents the quartic coupling term which is first order in ψ_s and cubic in d-wave components. We note that both $g_{sd} > 0$ and $g_{dd} > 0$ are taken to be positive so that relative $\pm\pi/2$ phase differences are energetically favored between any two of the three pairing components ψ_s, ψ_1, ψ_2. In what follows, by setting the phase of ψ_s to zero, we write

$$\psi_s = |\psi_s|, \quad \psi_1 = |\psi_1|e^{i\phi_1}, \quad \psi_2 = |\psi_2|e^{i\phi_2}, \tag{4}$$

in which $|\psi_s|$, $|\psi_1|$ and $|\psi_2|$ are magnitudes of the s-wave, $d_{x^2-y^2}$-wave, and d_{xy}-wave order parameters, and ϕ_1 and ϕ_2 are the phase differences of ψ_1 and ψ_2 relative to ψ_s. Notice that it is the term with coefficient g'_{sd}, which breaks the U(1) rotational symmetry down to C_{6v}. A more detailed derivation of Eq. (1) based on symmetry analysis is provided in Appendix A. The origin of the tricomponent form of the pairing gap function can be most evidently seen by retaining only the phase-sensitive terms in Eq. (1). Plugging the expressions of ψ_s, ψ_1 and ψ_2 in Eq. (4) into Eq. (1), we obtain

$$\begin{aligned} F = {} & f_1(|\psi_s|,|\psi_1|)\cos 2\phi_1 \\ & + f_2(|\psi_s|,|\psi_2|)\cos 2\phi_2 \\ & + f_0(|\psi_1|,|\psi_2|)\cos(2\phi_2 - 2\phi_1) \\ & + f_1'(|\psi_s|,|\psi_1|,|\psi_2|)\cos\phi_1 \\ & + f_2'(|\psi_s|,|\psi_1|,|\psi_2|)\cos(2\phi_2 - \phi_1), \end{aligned} \tag{5}$$

where

$$\begin{aligned} f_1(|\psi_s|,|\psi_1|) &= 2g_{sd}|\psi_s|^2|\psi_1|^2, \\ f_2(|\psi_s|,|\psi_2|) &= 2g_{sd}|\psi_s|^2|\psi_2|^2, \\ f_0(|\psi_1|,|\psi_2|) &= 2g_{dd}|\psi_1|^2|\psi_2|^2, \\ f_1'(|\psi_s|,|\psi_1|,|\psi_2|) &= 2g'_{sd}|\psi_s||\psi_1|(|\psi_1|^2 - 2|\psi_2|^2), \\ f_2'(|\psi_s|,|\psi_1|,|\psi_2|) &= -2g'_{sd}|\psi_s||\psi_1||\psi_2|^2. \end{aligned} \tag{6}$$

Since f_1, f_2, and f_0 are all positive, ϕ_1, ϕ_2 and $\phi_2 - \phi_1$ all tend to take values of $\pm\pi/2$, meaning that at least one of ϕ_1, ϕ_2, or $\phi_2 - \phi_1$ will deviate from $\pm\pi/2$.

Next we focus on the f_1' and f_2' terms in Eq. (5). Since g'_{sd} can be either positive or negative, the sign of f_1' is determined by the product of g'_{sd} and $(|\psi_1|^2 - 2|\psi_2|^2)$, while the sign of f_2' is determined by g'_{sd}. When $g'_{sd} > 0$, we have $f_2' < 0$, then $2\phi_2 - \phi_1$ tends to take values of $2n\pi$. In this case, if $|\psi_1|^2 - 2|\psi_2|^2 > 0$, then ϕ_1 tends to be $(2m+1)\pi$, resulting in $\phi_2 = (2m + 2n + 1)\pi/2$; whereas if $|\psi_1|^2 - 2|\psi_2|^2 < 0$, ϕ_1 tends to take the value of $2m\pi$, resulting in $\phi_2 = (m+n)\pi$, where both m and n are integers. A similar analysis can be performed for a negative g'_{sd}. The inclusion of the g'_{sd} term makes the competition between ϕ_1, ϕ_2 and $\phi_2 - \phi_1$ more complex, depending on the specific parameters taken in Eq. (1). Notice that it is impossible for ϕ_1 and ϕ_2 to satisfy all the constraints set by f_0, f_1, f_2, f_1', and f_2'.

For a full treatment, in order to determine the pattern of the three order parameters, an iterative numerical method is applied to obtain the solution of the pairing gap function by minimizing Eq. (1). The obtained results of pairing configurations are shown in Fig. 1. The parameters in free energy in Eq. (1) to obtain Fig. 1 are chosen as $\alpha_s = -N_F$, $\alpha_d = -3.179N_F$, $\beta_s = 2.635N_F/T_c^2$, $\beta_d = 0.790N_F/T_c^2$, $g_{dd} = 2.640N_F/T_c^2$, $g_{sd} = 0.275N_F/T_c^2$, and $g'_{sd} = -1.525N_F/T_c^2$, where N_F is the density of states at the Fermi level and T_c is the superconducting transition temperature. As previously discussed, the three parameters g_{dd}, g_{sd}, and g'_{sd} have significant impacts on the relative phases among different pairing components, thereby requiring careful consideration. On the other hand, γ is chosen to be 0 for simplification, as its value does not have a decisive influence on the relative phases and the symmetry breaking pattern. The obtained order parameters for this particular choice of parameters are $|\psi_s| = 0.604k_BT_c$, $|\psi_1| = 1.029k_BT_c$, $|\psi_2| = 0.962k_BT_c$, $\phi_1 = 0.383\pi$, and $\phi_2 = 0.835\pi$. We note that the phase difference between the two d-wave components is $\phi_2 - \phi_1 = 0.452\pi$, which is not equal to $\pi/2$ as in the chiral $d + id$ case.

The symmetry-breaking pattern of the configuration in Fig. 4(a_1) can be determined as

$$C_{6v} \times \mathbb{Z}_2^T \to C_2 \tag{7}$$

where $\mathbb{Z}_2^T$ is the $\mathbb{Z}_2$ group generated by time reversal operation. Eq. (7) is straightforward to be verified because the π-rotation around z axis takes x, y to $-x, -y$, resulting in $d_{x^2-y^2} \to d_{x^2-y^2}$ and $d_{xy} \to d_{xy}$. Except for C_2, all other symmetries are spontaneously broken in the ground state in Fig. 4(a_1). Since $|C_{6v} \times \mathbb{Z}_2^T|/|C_2| = 12$, where $|\ldots|$ represents the number of group elements, there are 12 degenerate solutions of the ground state pairing configura-

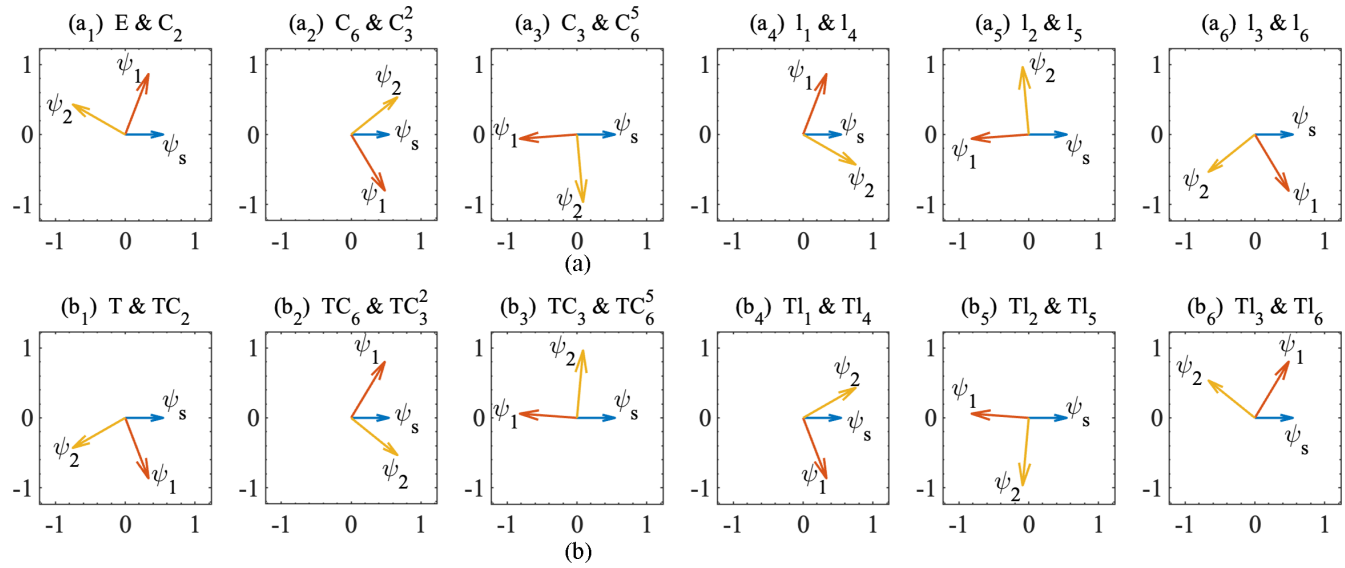

FIG. 4. Degenerate configurations of the tri-component-pairing $s + d_{x^2-y^2}e^{i\phi_1} + d_{xy}e^{i\phi_2}$. Symmetry operations which can generate the configuration from the one in (a_1) are indicated on top of each figure, where E is the identity operation; T is time reversal; $C_6, C_3, \ldots, C_6^5$ are rotations; and $l_1, l_2, \ldots, l_6$ are reflections. In all panels, ϕ_1 and ϕ_2 are not perpendicular with each other. In panels (a_3), (a_5), (b_3), and (b_5), ψ_1 and ψ_s are not exactly collinear, and ψ_2 is not precisely equal to $\pm\pi/2$. The parameters in Eq. (1) are chosen as $\alpha_s = -N_F$, $\alpha_d = -3.179N_F$, $\beta_s = 2.635N_F/T_c^2$, $\beta_d = 0.790N_F/T_c^2$, $\gamma = 0$, $g_{dd} = 2.640N_F/T_c^2$, $g_{sd} = 0.275N_F/T_c^2$, and $g'_{sd} = -1.525N_F/T_c^2$, where N_F is the density of states at the Fermi level and T_c is the superconducting transition temperature.

tions. The other eleven degenerate configurations are shown in Figs. 4(a_2)–4(a_6) and 4(b_1)–4(b_6), which can be obtained by performing the broken symmetry operations on the configuration in Fig. 4(a_1). The symmetry operations that can be used to generate the corresponding configuration from Fig. 4(a_1) are indicated on top of each subfigure in Fig. 4.

B. Other lattice symmetries

On the free energy level, degenerate $d_{x^2-y^2}$ and d_{xy} pairings can occur for other lattice symmetries as well, not just the C_{6v} symmetry considered in Sec. II A. In this subsection, we discuss the general forms of free energies when there is a coexistence of s-, $d_{x^2-y^2}$-, and d_{xy}-pairing components, focusing on the special cases for planar point groups where $d_{x^2-y^2}$- and d_{xy}-channels are degenerate, namely, they form a two-dimensional irreducible representation of the symmetry group.

It turns out that there are eight planar point group symmetries that satisfy the condition of degenerate $d_{x^2-y^2}$ and d_{xy} pairings, including C_{3v}, D_3, D_{3h}, D_{3d}, C_{6v}, D_6, D_{6h}, and D_{4d}. Among the eight point group symmetries, seven of them—from C_{3v} to D_{6h}—share the same form of free energy up to quartic order as the C_{6v} case given in Eq. (1), whereas the D_{4d} case has a different form, as summarized in Table I. More explicitly, the free energy F' for D_{4d} is given by

$$F' = F_s'^{(0)} + F_d'^{(0)} + F'^{(4)}, \tag{8}$$

in which

$$\begin{aligned} F_s'^{(0)} &= \alpha'_s|\psi_s|^2 + \beta'_s|\psi_s|^4, \\ F_d'^{(0)} &= \alpha'_d(|\psi_1|^2 + |\psi_2|^2) + \beta'_d(|\psi_1|^2 + |\psi_2|^2)^2, \end{aligned} \tag{9}$$

and

$$\begin{aligned} F'^{(4)} = {} & \gamma_{dd}|\psi_1|^2|\psi_2|^2 + \gamma_{sd}|\psi_s|^2(|\psi_1|^2 + |\psi_2|^2) \\ & + g'_{dd}\left(\psi_1^2\psi_2^{*2} + \psi_1^{*2}\psi_2^2\right) \\ & + g'_{sd}\left[\psi_s^{*2}\left(\psi_1^2 + \psi_2^2\right) + \psi_s^2\left(\psi_1^{*2} + \psi_2^{*2}\right)\right]. \end{aligned} \tag{10}$$

In this case, we also expect a mixture of $d_{x^2-y^2}$-, d_{xy}-, and s-wave pairing symmetries when $g'_{dd} > 0$ and $g'_{sd} > 0$ in Eq. (10).

TABLE I. Point groups with d_1-d_2 degeneracy and the corresponding free energy. The explicit forms of $F_s^{(0)}$, $F_d^{(0)}$, $F^{(4)}$, $F_s'^{(0)}$, $F_d'^{(0)}$, and $F'^{(4)}$ are given in Eqs. (2), (3), (9), and (10).

Symmetry groups	G-L free energy
$C_{3v}, D_3, D_{3h}, D_{3d}, C_{6v}, D_6, D_{6h}$	$F_s^{(0)} + F_d^{(0)} + F^{(4)}$
D_{4d}	$F_s'^{(0)} + F_d'^{(0)} + F'^{(4)}$

III. TOPOLOGICAL CHIRAL PAIRING

A. Microscopic model

Now we turn to a microscopic model. Retaining terms up to the nearest neighbors, it is direct to construct the Bogoliubov-de Gennes (BdG) Hamiltonian for the tricomponent superconducting pairing on a two-dimensional honeycomb lattice. The BdG Hamiltonian can be written as

$$H = \sum_{\boldsymbol{k}} \Psi_{\boldsymbol{k}}^\dagger h_{\boldsymbol{k}} \Psi_{\boldsymbol{k}}, \tag{11}$$

in which $\Psi_{\boldsymbol{k}} = (c_{\boldsymbol{k}_A,\uparrow}\, c_{\boldsymbol{k}_B,\uparrow}\, c^\dagger_{-\boldsymbol{k}_A,\downarrow}\, c^\dagger_{-\boldsymbol{k}_B,\downarrow})^T$, where $c^\dagger_{\boldsymbol{k}_j,\sigma}$ and $c_{\boldsymbol{k}_j,\sigma}$ represent the creation and annihilation operators, respectively, for an electron with momentum $\boldsymbol{k} = (k_x, k_y)$ and spin σ in the sublattice $j = A, B$; $h_{\boldsymbol{k}}$ is the 4×4 BdG Hamiltonian matrix containing the normal-state Hamiltonian $H_0(\boldsymbol{k})$ and the

pairing term $\Delta(\boldsymbol{k})$, given by

$$h_{\boldsymbol{k}} = \begin{pmatrix} H_0(\boldsymbol{k}) & \Delta(\boldsymbol{k}) \\ \Delta^\dagger(\boldsymbol{k}) & -H_0^T(-\boldsymbol{k}) \end{pmatrix}. \tag{12}$$

In the absence of a staggered potential [86–88], the normal-state Hamiltonian can be expressed as

$$H_0(\boldsymbol{k}) = \epsilon_x(\boldsymbol{k})\sigma_x + \epsilon_y(\boldsymbol{k})\sigma_y - \mu\sigma_0, \tag{13}$$

where

$$\epsilon_x(\boldsymbol{k}) = -t\sum_{i=1}^{3}\cos(\boldsymbol{k}\cdot\boldsymbol{a}_i),$$
$$\epsilon_y(\boldsymbol{k}) = t\sum_{i=1}^{3}\sin(\boldsymbol{k}\cdot\boldsymbol{a}_i), \tag{14}$$

in which σ_α ($\alpha = x, y, z$) are 2×2 Pauli matrices that encode the sublattice degree of freedom, σ_0 is the 2×2 identity matrix, μ is the chemical potential, t is the nearest-neighbor hopping amplitude, and $\boldsymbol{a}_i$ ($i = 1, 2, 3$) are vectors defined in Fig. 2. The Hamiltonian $H_0(\boldsymbol{k})$ describes the kinetic energy and nearest-neighbor hopping of electrons in the non-superconducting state of the system.

Considering the superconducting pairing in the chiral spin-singlet state, the tri-component-pairing term can be expressed as

$$\Delta(\boldsymbol{k}) = \Delta_s(\boldsymbol{k}) + \Delta_{x^2-y^2}(\boldsymbol{k})e^{i\phi_1} + \Delta_{xy}(\boldsymbol{k})e^{i\phi_2}, \tag{15}$$

where

$$\Delta_s(\boldsymbol{k}) = |\psi_s|\sigma_0, \tag{16}$$

and

$$\Delta_{x^2-y^2}(\boldsymbol{k}) = |\psi_1|\left\{\left[\cos(k_x a) - \cos\left(\frac{1}{2}k_x a\right)\cos\left(\frac{\sqrt{3}}{2}k_y a\right)\right]\sigma_x - \left[\sin(k_x a) + \sin\left(\frac{1}{2}k_x a\right)\cos\left(\frac{\sqrt{3}}{2}k_y a\right)\right]\sigma_y\right\},$$
$$\Delta_{xy}(\boldsymbol{k}) = \sqrt{3}|\psi_2|\left\{\left[-\sin\left(\frac{1}{2}k_x a\right)\sin\left(\frac{\sqrt{3}}{2}k_y a\right)\right]\sigma_x + \left[\cos\left(\frac{1}{2}k_x a\right)\sin\left(\frac{\sqrt{3}}{2}k_y a\right)\right]\sigma_y\right\}. \tag{17}$$

According to the calculations in Appendix B, $(\Delta_{x^2-y^2}, \Delta_{xy})$ transform in the same way as $(d_{x^2-y^2}, d_{xy})$ under the C_{6v} group. Hence $(\Delta_{x^2-y^2}, \Delta_{xy})$ represent d-wave pairings for the discrete symmetry group C_{6v}.

Substituting Eqs. (16) and (17) into Eq. (15), we obtain

$$\Delta(\boldsymbol{k}) = \Delta_s\sigma_0 + \Delta_x(\boldsymbol{k})\sigma_x + \Delta_y(\boldsymbol{k})\sigma_y, \tag{18}$$

where

$$\Delta_s = |\psi_s|, \tag{19}$$

and

$$\Delta_x(\boldsymbol{k}) = |\psi_1|e^{i\phi_1}\left[\cos(k_x a) - \cos\left(\frac{1}{2}k_x a\right)\cos\left(\frac{\sqrt{3}}{2}k_y a\right)\right] - \sqrt{3}|\psi_2|e^{i\phi_2}\left[\sin\left(\frac{1}{2}k_x a\right)\sin\left(\frac{\sqrt{3}}{2}k_y a\right)\right],$$
$$\Delta_y(\boldsymbol{k}) = -|\psi_1|e^{i\phi_1}\left[\sin(k_x a) + \sin\left(\frac{1}{2}k_x a\right)\cos\left(\frac{\sqrt{3}}{2}k_y a\right)\right] + \sqrt{3}|\psi_2|e^{i\phi_2}\left[\cos\left(\frac{1}{2}k_x a\right)\sin\left(\frac{\sqrt{3}}{2}k_y a\right)\right]. \tag{20}$$

The 4×4 BdG Hamiltonian can be expressed as

$$h_{\boldsymbol{k}} = [\mathrm{Re}(\Delta_x)\sigma_x + \mathrm{Re}(\Delta_y)\sigma_y + \Delta_s\sigma_0]\tau_x - [\mathrm{Im}(\Delta_x)\sigma_x + \mathrm{Im}(\Delta_y)\sigma_y]\tau_y + (\epsilon_x\sigma_x + \epsilon_y\sigma_y - \mu\sigma_0)\tau_z, \tag{21}$$

where τ_α ($\alpha = x, y, z$) are the Pauli matrices in the particle-hole channel. Diagonalization of $h_{\boldsymbol{k}}$ gives two pairs of energy eigenvalues $\pm E_i(\boldsymbol{k})$ for each momentum $\boldsymbol{k}$,

$$E_i(\boldsymbol{k}) = \sqrt{|\Delta_x|^2 + |\Delta_y|^2 + |\Delta_s|^2 + \epsilon_x^2 + \epsilon_y^2 + \mu^2 + (-)^i D_{\boldsymbol{k}}}, \tag{22}$$

where $i = 1, 2$ and

$$D_{\boldsymbol{k}}^2 = 4\mu^2(\epsilon_x^2 + \epsilon_y^2) + 2|\Delta_x|^2|\Delta_y|^2 - (\Delta_x^2\Delta_y^{*2} + \Delta_y^2\Delta_x^{*2}) + 4[\epsilon_x^2|\Delta_y|^2 + \epsilon_y^2|\Delta_x|^2 - \epsilon_x\epsilon_y(\Delta_x\Delta_y^* + \Delta_y\Delta_x^*)] + \Delta_s^2[(\Delta_x + \Delta_x^*)^2 + (\Delta_y + \Delta_y^*)^2] - 8\mu\Delta_s[\epsilon_x\mathrm{Re}(\Delta_x) + \epsilon_y\mathrm{Re}(\Delta_y)]. \tag{23}$$

The plots of $E_1(\boldsymbol{k})$ and $E_2(\boldsymbol{k})$ are depicted in Fig. 5 by taking $|\psi_s| = 0.0604t$, $|\psi_1| = 0.1029t$, $|\psi_2| = 0.0962t$, $\phi_1 = 0.383\pi$, $\phi_2 = 0.835\pi$, and $\mu = -0.4t$, which give a fully gapped energy spectrum. To more clearly demonstrate the gap, Fig. 5(c) is created by fixing $k_y = 4\pi/(3\sqrt{3}a)$ (which is the y coordinate of the K point) and plotting the curves of $\pm E_{1,2}(\boldsymbol{k})$ as functions of k_x only. It is evident that a gap exists at the Dirac point $K = (0, \frac{4\pi}{3\sqrt{3}a})$, where $E \approx \pm 0.454t$ and the gap size $\delta E \approx 0.103t$.

B. Chern number

A nonvanishing Chern number is the signature of a non-trivial topological property for two-dimensional systems, which is defined as [89,90]

$$C = \frac{1}{2i\pi}\int d^2k F_{xy}(\boldsymbol{k}), \tag{24}$$

in which the Berry connection $A_\alpha(\boldsymbol{k})(\alpha = x, y)$ and the associated field strength $F_{xy}(\boldsymbol{k})$ are given by

$$A_\alpha(\boldsymbol{k}) = \langle n(\boldsymbol{k})|\partial_\alpha|n(\boldsymbol{k})\rangle,$$
$$F_{xy}(\boldsymbol{k}) = \partial_x A_y(\boldsymbol{k}) - \partial_y A_x(\boldsymbol{k}), \tag{25}$$

where $|n(\boldsymbol{k})\rangle$ is a normalized wave function of the nth energy band. With the opening of the mass gap, the four eigenstates of the BdG Hamiltonian in Eq. (21) are everywhere nondegenerate, so that a Chern number C_n can be defined for each band n as labeled in Fig. 5(c). At $T = 0$ K, the Chern numbers for corresponding energy bands are calculated as $C_1 = 1$, $C_2 = -3$, $C_3 = 3$, and $C_4 = -1$, using the numerical method

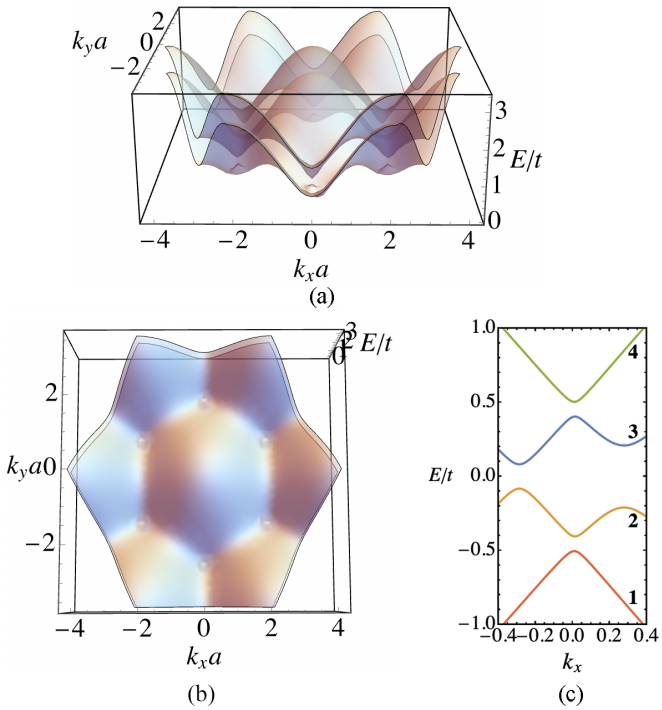

FIG. 5. Eigenvalues of the BdG Hamiltonian in Eq. (21). (a) Presents three-dimensional plots of the positive E_1 and E_2 as functions of $\boldsymbol{k}$, where a gap opens at the Dirac points. (b) Provides a top view of (a). (c) Illustrates the variation of the four eigenvalues with respect to k_x, with the k_y coordinate fixed to be the y component of the K point. In all plots, we set $|\psi_s| = 0.0604t$, $|\psi_1| = 0.1029t$, $|\psi_2| = 0.0962t$, $\phi_1 = 0.383\pi$, $\phi_2 = 0.835\pi$, and $\mu = -0.4t$.

proposed in Refs. [91,92]. The choices of order parameters and chemical potential are the same as in Fig. 5, corresponding to Fig. 4(a_1). The sum of the Chern numbers of the two occupied bands (i.e., $n = 1, 2$) is -2, which is consistent with the characteristics of a chiral d-wave superconductivity.

The behavior of the Chern numbers under the transformations of the $C_{6v} \times \mathbb{Z}_2^T$ group elements is illustrated in Fig. 6. If $\phi_2 - \phi_1 < \pi$, the Chern numbers are given by $C_1 = 1$, $C_2 = -3$, $C_3 = 3$, $C_4 = -1$, and the sum of the Chern numbers of the bands with negative energies is -2; conversely,

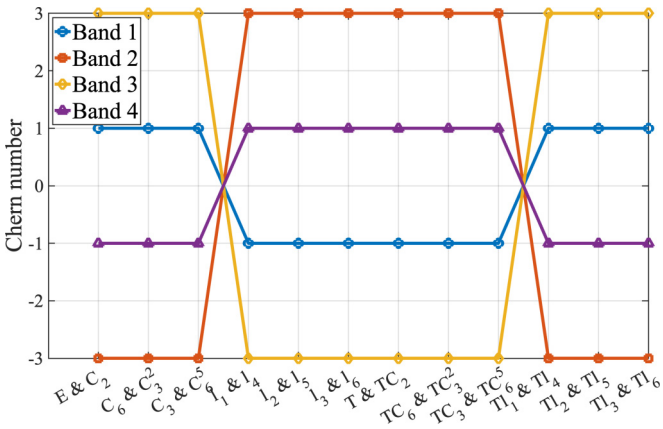

FIG. 6. Evolution of Chern numbers under symmetry operations in $C_{6v} \times \mathbb{Z}_2^T$.

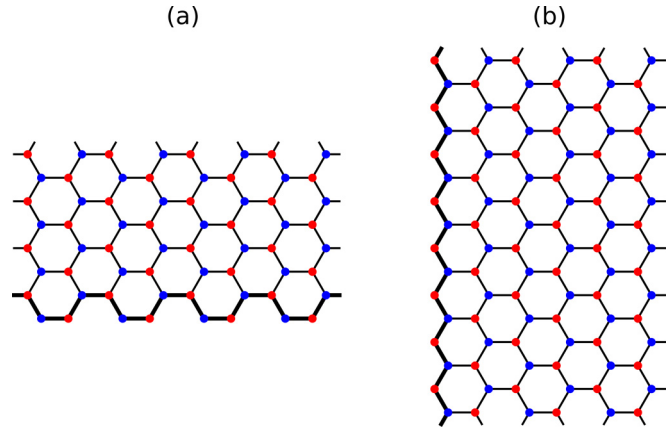

FIG. 7. Plots for (a) armchair and (b) zigzag edges on the honeycomb lattice, in which the thickened bonds represent the bonds on the edges.

if $\phi_2 - \phi_1 > \pi$, the Chern numbers change sign, and the sum is 2. It can be observed that rotational transformations do not alter the Chern numbers, while mirror reflection and time-reversal transformations reverse the sign of the Chern numbers.

C. Edge states

When Chern number is nonzero, it is expected that chiral edge states emerge on the boundaries of the system [93,94], which, for the case of topological superconductors, are Majorana modes propagating unidirectionally along the sample boundaries [2,10,12–14,95–97].

To further study the topological properties of the obtained tri-component superconducting pairing $s + d_{x^2-y^2} e^{i\phi_1} + d_{xy} e^{i\phi_2}$, we solve edge states for different boundary geometries, namely, armchair, and zigzag as shown in Fig. 7, by taking the 1D edge direction of the two-dimensional honeycomb lattice to be periodic and the perpendicular direction to be open and finite with 100 unit cells of the honeycomb lattice. Figures 8(a) and 8(b) display the numerical results for the energy spectrum for armchair

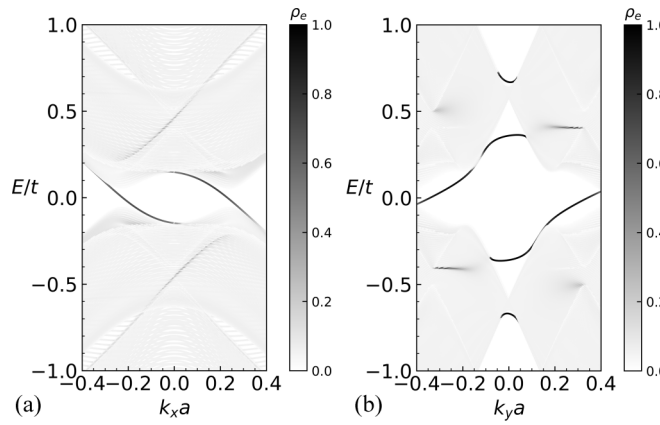

FIG. 8. Energy spectrum for (a) armchair edge and (b) zigzag edge. ρ_es are the integrated wave-function probabilities in the first ten stripes of unit cells close to the boundaries. The choices of order parameters and chemical potential are the same as in Fig. 5.

and zigzag boundaries, respectively, in which the horizontal axes are the momenta in the periodic directions, namely, k_x for armchair and k_y for zigzag (for definition of x and y directions, see Fig. 2), and the vertical axis is the exictation energy E in units of hopping t. The grey scales ρ_e in Figs. 8(a) and 8(b) are defined as

$$\rho_e = \sum_{j=1}^{10} \sum_{\lambda=A,B} \sum_{\sigma=\uparrow,\downarrow} |\psi_\sigma(j,\lambda)|^2, \tag{26}$$

in which j is the index of the stripe of unit cells measured from the edge in the direction perpendicular to the edge, λ is the index for sublattice sites within a unit cell, σ is the spin index, and $\psi_\sigma(j,\lambda)$ is the wave function for the corresponding eigenstate. Notice that ρ_e represents the integrated wave function probabilities in the first ten stripes of unit cells close to the boundaries, thereby can be used for calibrating the degree of localization of the wave functions near the boundaries.

As can be seen from Fig. 8(a), two well-defined dispersive mid-gap modes can be clearly observed for the armchair case. The relatively dark colors of the two mid-gap lines undoubtedly hint at their edge state nature. Moreover, the two chiral edge modes both cross $E = 0$ in Fig. 8(a), consistent with a total Chern number of the two negative energy bands being equal to ± 2. As for the case of the zigzag edge shown in Fig. 8(b), two chiral edge modes crossing $E = 0$ can also be observed, again consistent with the bulk Chern number.

IV. ANISOTROPIC ac HALL CONDUCTIVITY

Under the influence of incident light, the refractive index of a material changes, which in turn alters the polarization state of the light. This is known as the optical Kerr effect [98,99], and the angle of polarization change is called the Kerr angle, which can be used as a signal for chiral topological phase [100,101]. In the optical Kerr effect, we focus on the interaction between light and matter, which is influenced by the anomalous ac Hall conductivity $\sigma_H(\omega)$ [102–104]. The Kerr angle, θ_K, is directly related to $\sigma_H(\omega)$, and as a result, the presence of $\sigma_H(\omega)$ can be used as an experimental signature for the existence of time-reversal symmetry breaking.

A. Expression for ac Hall conductivity

The anomalous ac Hall conductivity is the antisymmetric part of the optical Hall conductivity,

$$\sigma_H(\omega) = \tfrac{1}{2} \lim_{\boldsymbol{q}\to 0} [\sigma_{xy}(\boldsymbol{q},\omega) - \sigma_{yx}(\boldsymbol{q},\omega)], \tag{27}$$

in which ω is the frequency of the incident light, and the optical Hall conductivity $\sigma_{xy}(\boldsymbol{q}, w)$ is related to the current-current correlator $\pi_{xy}(\boldsymbol{q},\omega)$ via

$$\sigma_{xy}(\boldsymbol{q},\omega) = \frac{1}{\hbar\omega}\pi_{xy}(\boldsymbol{q},\omega). \tag{28}$$

The current-current correlator $\pi_{xy}(\boldsymbol{q},\omega)$ is defined as

$$\pi_{xy}(\boldsymbol{q},\omega) = \int_0^\infty dt\, e^{i\omega t} \langle [\hat{J}_x^\dagger(\boldsymbol{q},t), \hat{J}_y(\boldsymbol{q},0)] \rangle, \tag{29}$$

in which $\hat{J}_\alpha = e\sum_{\boldsymbol{k}} \Psi_{\boldsymbol{k}}^\dagger \hat{v}_\alpha \Psi_{\boldsymbol{k}}$ is the α'th component ($\alpha = x, y$) of the current operator, and $\hat{v}_\alpha$ is the α'th component of the velocity operator in Nambu notation given by

$$\hat{v}_\alpha = \frac{1}{\hbar}(\sigma_z \otimes \sigma_0)\partial_{k_\alpha} h_{\boldsymbol{k}}^0, \tag{30}$$

where $h_{\boldsymbol{k}}^0$ is the normal part of the BdG Hamiltonian in Eq. (21), namely,

$$h_{\boldsymbol{k}}^0 = (-\mu\sigma_0 + \epsilon_x\sigma_x + \epsilon_y\sigma_y)\tau_z. \tag{31}$$

Under time-reversal transformation, the current correlator changes as $\pi_{xy} \to \pi_{yx}$; and under mirror reflection transformation along $\hat{x}$ or $\hat{y}$ axis, the current correlator changes as $\pi_{xy} \to -\pi_{xy}$ (for details, see Appendix C), both of which result in a sign change of σ_H. Therefore, if either of the two above symmetries is unbroken, σ_H must be zero in order to preserve the invariance of the observable quantity. Hence, to obtain a nonzero ac Hall conductivity, both time-reversal and mirror symmetries along the $\hat{x}$ and $\hat{y}$ axes must be broken.

Specifically, in superconducting systems with a multiband feature and a symmetry-breaking pattern of $C_{6v} \times \mathbb{Z}_2^T \to C_2$ as described by Eq. (21), the condition for generating a nonzero σ_H is fulfilled. A straightforward evaluation from Eqs. (27)–(31) yields the anomalous ac Hall conductivity as follow,

$$\sigma_H(\omega) = \lim_{i\nu_m\to\omega+i\epsilon} \frac{e^2}{\hbar\beta} \int \frac{d^2k}{(2\pi)^2} \sum_{\omega_n} \frac{2\hbar^3(\nu_m+2\omega_n)^2(v_x^* v_y - v_x v_y^*)[\mu(\Delta_x^*\Delta_y - \Delta_x\Delta_y^*) + 2i\Delta_s(\epsilon_x \mathrm{Im}\Delta_y - \epsilon_y \mathrm{Im}\Delta_x)]}{\left(\hbar^2\omega_n^2 + E_1^2\right)\left(\hbar^2\omega_n^2 + E_2^2\right)\left[\hbar^2(\omega_n+\nu_m)^2 + E_1^2\right]\left[\hbar^2(\omega_n+\nu_m)^2 + E_2^2\right]}. \tag{32}$$

where ν_m is the bosonic Matsubara frequency, ω_n is the fermionic Matsubara frequency, $\beta = 1/k_B T$, $v_\alpha = (1/\hbar)\partial_{k_\alpha}(\epsilon_x - i\epsilon_y)$, $\alpha = x, y$, and ϵ represents a positive infinitesimal here. For the tri-component-pairing state $s + d_{x^2-y^2}e^{i\phi_1} + d_{xy}e^{i\phi_2}$ with time-reversal symmetry breaking, the leading term of the vertex correction is zero and thus can be neglected [105]. Detailed derivation of Eq. (32) is included in Appendix D. The reason why $\sigma_H(\omega)$ is nonzero can be directly seen from Eq. (32) as follows. In order for the Hall signal to be non-vanishing, the integrand in Eq. (32) must be even under the reflection $x \leftrightarrow y$. Indeed, the eigen-energy E_α in the denominator remains unchanged under the exchange of the x and y indices, whereas the terms involving $(v_x^* v_y - v_x v_y^*)$, $(\Delta_x\Delta_y^* - \Delta_x^*\Delta_y)$, and $(\epsilon_x \mathrm{Im}\Delta_y - \epsilon_y \mathrm{Im}\Delta_x)$ in the numerator

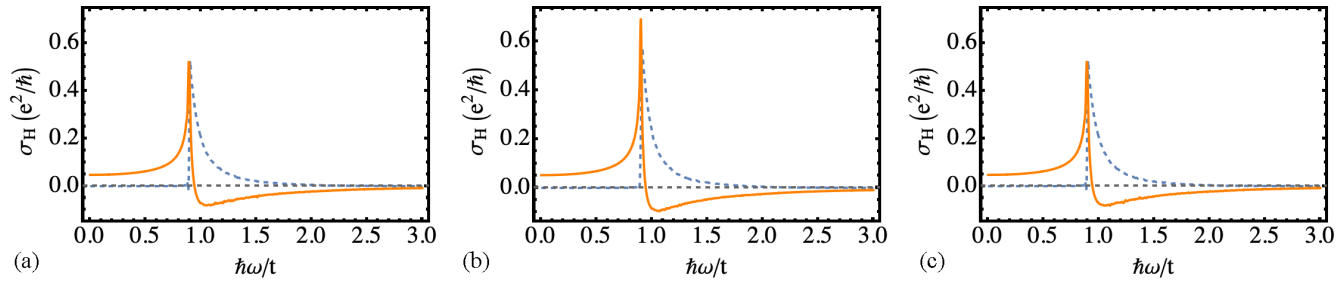

FIG. 9. Anisotropy of the real (solid line) and imaginary (dashed line) parts of the anomalous ac Hall conductivity in Eq. (32). (a) Shows the line-shape for $\sigma_H(\omega)$ without any symmetry operations, (b) and (c) present the line-shapes for $\sigma_H(\omega)$ when the coordinate axes are rotated by $\pi/3$ and $2\pi/3$ angles around the z axis, respectively. Both real part and imaginary part in all panels reach a peak at $\hbar\omega \approx 0.9t$. The fact that $\sigma_H \neq 0$ demonstrates that the system is in a chiral topological superconducting phase, and the change in σ_H after rotation in (b) and (c) reflects the anisotropy of the anomalous ac Hall conductivity under the tri-component-pairing configuration. In this figure, we use the same parameters as in Fig. 5, and set the temperature $k_BT = 0.01t$.

change sign under $x \leftrightarrow y$, so that the overall numerator is also even. As a result, Eq. (32) satisfies the condition for generating a non-vanishing ac Hall conductivity.

B. Numerical results for ac Hall conductivity

The line-shapes for both the real and imaginary parts of $\sigma_H(\omega)$ as functions of ω are plotted in Fig. 9(a), where the same parameters for the chemical potential and superconducting pairing are used as in Fig. 5, and the temperature is set to be $k_BT = 0.01t$. From Fig. 9(a), it can be observed that when the incident light energy satisfies $\hbar\omega = [E_1(\boldsymbol{k}) + E_2(\boldsymbol{k})]_{\min} \approx 0.9t$, both $\mathrm{Re}(\sigma_H)$ and $\mathrm{Im}(\sigma_H)$ exhibit peaks. The peak position in $\mathrm{Im}(\sigma_H)$ can be understood from resonances. Notice that $\mathrm{Im}(\sigma_H)$ contains delta-functions $\delta(E_1 + E_2 + \hbar\omega)$ and $\delta(E_1 + E_2 - \hbar\omega)$ (see Appendix D for details). The energy conservation constraint in $\delta(E_1 + E_2 + \hbar\omega)$ cannot be satisfied for positive ω, and the constraint in $\delta(E_1 + E_2 - \hbar\omega)$ can be satisfied only when ω is above the two-particle continuum, i.e., $\hbar\omega \geqslant [E_1(\boldsymbol{k}) + E_2(\boldsymbol{k})]_{\min}$. This is the reason for the onset of a nonzero $\mathrm{Im}(\sigma_H)$ at $[E_1(\boldsymbol{k}) + E_2(\boldsymbol{k})]_{\min}$, where a peak shows up due to an enhancement of the density of states. On the other hand, $\mathrm{Re}(\sigma_H)$ is related to $\mathrm{Im}(\sigma_H)$ through the Kramers-Kronig relation,

$$\mathrm{Re}[\sigma_H(\omega)] = \frac{1}{\pi}\mathcal{P}\int_{-\infty}^{\infty}\frac{\mathrm{Im}[\sigma_H(\omega')]}{\omega' - \omega}d\omega', \tag{33}$$

which means that if a peak appears in the imaginary part at a certain frequency, the real part will inevitably undergo significant changes in the nearby frequency range, and it is highly likely to also form a peak.

In addition, the temperature dependence of the anomalous ac Hall conductivity without any symmetry operations is shown in Fig. 10. For clearer numerical variation, the frequency is chosen near the peak value of σ_H in Fig. 9(a), i.e., $\hbar\omega = 0.9t$. As the temperature increases from 0 to the superconducting critical temperature T_c, both the real and imaginary parts of σ_H decrease gradually, with a slow decay near $T = 0$ and a faster decay close to T_c. We note that for the σ_H curves with any symmetry operation, fixing the frequency at an arbitrary value should yield a temperature dependence of σ_H similar to that shown in Fig. 10.

A nonvanishing $\sigma_H(\omega)$ leads to Kerr effect in the material, which can be used as an experimental signature for detecting time reversal symmetry breaking. When polarized light is incident on the surface of a chiral topological superconductor, the polarization direction of the reflected light undergoes rotation due to the nonzero ac Hall conductivity of the material. For thick samples ($h \gg \lambda$), the Kerr angle θ_K depends on $\sigma_H(\omega)$ as follows [98]:

$$\theta_K(\omega) = \frac{2\pi}{d\omega}\mathrm{Im}\left(\frac{\sigma_H(\omega)}{n(n^2-1)}\right), \tag{34}$$

where λ is the wavelength of the incident light, and d denotes the separation of monolayer pairs. And for thin samples ($h \ll \lambda$), the Kerr angle is given by [80],

$$\theta_K(\omega) = \mathrm{Re}\arctan\left(\frac{-\sigma_H}{\sigma_{xx} + 4\pi\left(\sigma_{xx}^2 + \sigma_H^2\right)}\right), \tag{35}$$

where σ_{xx} is the longitudinal optical conductivity.

C. Comparison with $d + id$ pairing and breaking of rotational symmetry

We emphasize that the behavior of ac Hall conductivity for the tri-component $s + d_{x^2-y^2}e^{i\phi_1} + d_{xy}e^{i\phi_2}$ pairing exhibits notable differences compared with the chiral d-wave one $d_{x^2-y^2} + id_{xy}$. In the chiral d-wave case, σ_H vanishes at the Dirac point where the chemical potential $\mu = 0$. On the other hand, σ_H is nonvanishing even at the Dirac point for the

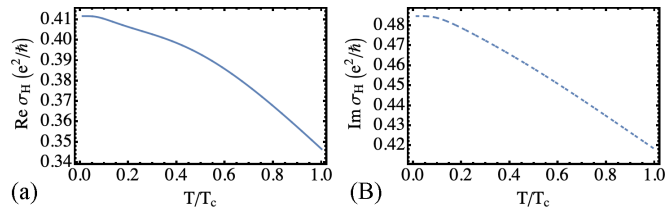

FIG. 10. Real (panel (a)) and imaginary (panel (b)) parts of the anomalous ac Hall conductivity for $s + d_{x^2-y^2}e^{i\phi_1} + d_{xy}e^{i\phi_2}$ pairing as functions of the temperature. Same order parameters and chemical potential are taken as in Fig. 9, and the frequency is set to be $\hbar\omega = 0.9t$.

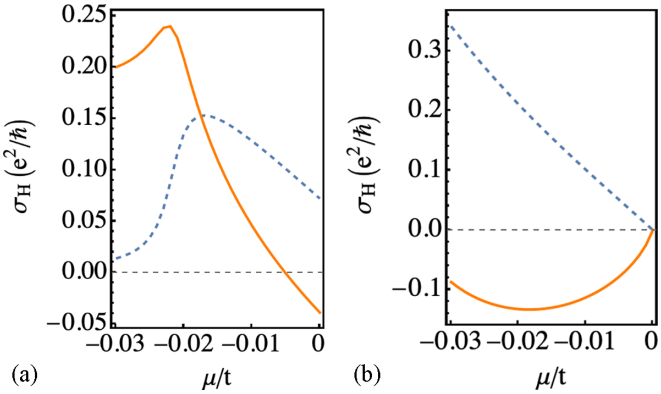

FIG. 11. Real (solid line) and imaginary (dashed line) parts of the anomalous ac Hall conductivity for (a) $s + d_{x^2-y^2}e^{i\phi_1} + d_{xy}e^{i\phi_2}$ pairing, and (b) $d_{x^2-y^2} + id_{xy}$ pairing gap function, as functions of chemical potential. In (a), the same parameters for the tri-component-pairing are used as in Fig. 5, while in (b), $|\psi_{x^2-y^2}| = |\psi_{xy}| = 0.1t$. It is worth noting that in (a), σ_H for the tri-component-pairing is nonzero at $\mu = 0$, with a value of $(-0.0387 + 0.0723i)e^2/\hbar$, while σ_H for the $d + id$ pairing completely vanishes at $\mu = 0$. In all plots, we set $k_BT = 0.01t$ with mixed $\hbar\omega = 0.35t$.

$s + d_{x^2-y^2}e^{i\phi_1} + d_{xy}e^{i\phi_2}$ pairing, because of the presence of the $\Delta_s(\epsilon_x \mathrm{Im}\Delta_y - \epsilon_y \mathrm{Im}\Delta_x)$ term in the numerator of Eq. (32), as shown in Fig. 11.

It is noted that, for the parameter choices in the figure, the anomalous ac Hall conductivity of the tricomponent pairing exhibits a single peak in both the real and imaginary parts within the range $-0.03t \leqslant \mu \leqslant 0$, whereas the curve for the $d + id$ pairing gradually approaches zero. The origin of the peak in Fig. 11(a) is essentially the same as those in Fig. 9. Specifically, when $\hbar\omega = 0.35t$ is fixed, the peak position μ_{peak} satisfies $(E_1 + E_2)_{\mathrm{min}} = 0.35t = \hbar\omega$. At this threshold, $\mathrm{Im}(\sigma_H)$ exhibits a peak due to an enhancement of the density of states, and $\mathrm{Re}(\sigma_H)$ follows via the Kramers–Kronig relation. For $|\mu| > |\mu_{\mathrm{peak}}|$, one has $(E_1 + E_2)_{\mathrm{min}} > 0.35t$, and σ_H has not yet attained its maximum. For $|\mu| < |\mu_{\mathrm{peak}}|$, $(E_1 + E_2)_{\mathrm{min}} < 0.35t$, leading to a gradual decrease after the peak, including a region where $\mathrm{Re}(\sigma_H) < 0$, consistent with Fig. 9. By contrast, for the $d + id$ pairing in Fig. 11(b), at $\mu = -0.03t$ one already has $(E_1 + E_2)_{\mathrm{min}} < 0.35t$, and this inequality persists as $|\mu|$ decreases further. Consequently, σ_H exhibits no peak and gradually approaches zero.

Furthermore, unlike the chiral d-wave pairing, the ac Hall conductivity for the $s + d_{x^2-y^2}e^{i\phi_1} + d_{xy}e^{i\phi_2}$ pairing is not invariant under the C_6 rotational operation, since C_6 symmetry is spontaneously broken in the tri-component case. Figures 9(b) and 9(c) show the line shapes of $\mathrm{Re}[\sigma_H(\omega)]$ and $\mathrm{Im}[\sigma_H(\omega)]$ when the coordinate axes are rotated by $\pi/3$ and $2\pi/3$ angles around the z axis, respectively. Namely, the $\hat{x}$ and $\hat{y}$ directions in Eq. (32) for calculating $\sigma_H(\omega)$ are replaced by $\hat{x}'$ and $\hat{y}'$ directions, where $(\hat{x}', \hat{y}')$ are obtained from $(\hat{x}, \hat{y})$ by a rotation of angle $\pi/3$ for Fig. 9(b) and $2\pi/3$ for Fig. 9(c). It is evident from Figs. 9(a)–9(c) that the line shapes are different for the three setups, indicating an anisotropy in the ac Hall response of the system along different directions. Such anisotropy can be used as an experimental probe to distinguish between chiral $d + id$ pairing and the tricomponent $s + d_{x^2-y^2}e^{i\phi_1} + d_{xy}e^{i\phi_2}$ pairing.

V. FRACTIONAL VORTICES IN MAGNETIC FIELDS

In this section, we discuss another physical property of the tri-component-pairing with mixed $d_{x^2-y^2}$-, d_{xy}-, and s-wave symmetries—fractional vortices, which occur in multicomponent pairing systems [82].

To study vortex structures in superconductors, the spatial gradient terms of order parameters and magnetic fields need to be included in the Ginzburg-Landau free energy. By incorporating these effects, the free energy functional can be written as

$$F = F_s^{(0)} + F_d^{(0)} + F^{(4)} + \frac{\mathbf{B}^2}{2} + \frac{1}{2m_s}|(\nabla + 2ie\mathbf{A})\psi_s|^2 + \frac{1}{2m_1}|(\nabla + 2ie\mathbf{A})\psi_1|^2 + \frac{1}{2m_2}|(\nabla + 2ie\mathbf{A})\psi_2|^2, \quad (36)$$

in which the expressions for $F_s^{(0)}$ and $F_d^{(0)}$ are the same as in Eq. (2), and $F^{(4)}$ is given in Eq. (3). Here, $m_{s,1,2}$ are the effective masses of the Cooper pairs associated with the order parameters $\psi_{s,1,2}$, e is the electron charge, and the order parameters are coupled to the vector potential $\mathbf{A}$ via minimal coupling. Performing the functional derivative of Eq. (36) with respect to the vector potential $\mathbf{A}$ (for details, see Appendix E), we obtain the expression of the supercurrent as

$$\mathbf{J} = -4e\rho^2\left[\cos^2\left(\frac{\theta}{2}\right)\nabla\phi_s + \sin^2\left(\frac{\theta}{2}\right)\cos^2\left(\frac{\gamma}{2}\right)\nabla\phi_1 + \sin^2\left(\frac{\theta}{2}\right)\sin^2\left(\frac{\gamma}{2}\right)\nabla\phi_2 + 2e\mathbf{A}\right], \quad (37)$$

in which

$$\rho^2 = \frac{|\psi_s|^2}{2m_s} + \frac{|\psi_1|^2}{2m_1} + \frac{|\psi_2|^2}{2m_2}, \quad (38)$$

and θ and γ are given by

$$|\psi_s| = \sqrt{2m_s}\rho\cos\left(\frac{\theta}{2}\right),$$
$$|\psi_1| = \sqrt{2m_1}\rho\sin\left(\frac{\theta}{2}\right)\cos\left(\frac{\gamma}{2}\right),$$
$$|\psi_2| = \sqrt{2m_2}\rho\sin\left(\frac{\theta}{2}\right)\sin\left(\frac{\gamma}{2}\right). \quad (39)$$

In the far-field region, i.e., at distances away from the vortex core much larger than the magnetic penetration length λ, the supercurrent vanishes. Therefore, integrating over a closed path σ around the vortex core in the far-field region gives

$$\oint_\sigma d\boldsymbol{l}\cdot\mathbf{J} = 0. \quad (40)$$

Then we arrive at the following equation for the magnetic flux $\Phi = \oint_\sigma d\boldsymbol{l}\cdot\mathbf{A}$ carried by the vortex:

$$\Phi = -\frac{1}{2e}\left[\cos^2\left(\frac{\theta}{2}\right)\Delta\phi_s + \sin^2\left(\frac{\theta}{2}\right)\cos^2\left(\frac{\gamma}{2}\right)\Delta\phi_1 + \sin^2\left(\frac{\theta}{2}\right)\sin^2\left(\frac{\gamma}{2}\right)\Delta\phi_2\right], \quad (41)$$

where $\Delta\phi_{s,1,2} = \oint_\sigma d\boldsymbol{l}\cdot\nabla\phi_{s,1,2}$ are the phase windings of the order parameters. It then follows that depending on the

values of $\Delta\phi_s$, $\Delta\phi_1$, and $\Delta\phi_2$, vortices in tri-component-pairing superconducting system can carry either integer or arbitrary fractional magnetic flux quanta. Specifically, when $\Delta\phi_s = \Delta\phi_1 = \Delta\phi_2 = 2n\pi$, the magnetic flux of the vortex is $\Phi = -n\Phi_0$, where $\Phi_0 = \pi/e$ denotes the standard flux quantum. In this case, the vortices are the Abrikosov vortices of an ordinary superconductor, each carrying n flux quanta.

If $\Delta\phi_1 = \Delta\phi_2 = 2n\pi$ and $\Delta\phi_s + \Delta\phi_1 = 0$, the magnetic flux becomes

$$\Phi = -\frac{1}{2e}\left[-\cos^2\left(\frac{\theta}{2}\right)\Delta\phi_1 + \sin^2\left(\frac{\theta}{2}\right)\Delta\phi_1\right] = \cos\theta n\Phi_0. \tag{42}$$

Since $\cos\theta$ can take an arbitrary value, such a vortex can carry an arbitrary fraction of the magnetic flux quantum, similar to the case in two-component superconductors. Likewise, if $\Delta\phi_1 = \Delta\phi_s = 2n\pi$ and $\Delta\phi_1 + \Delta\phi_2 = 0$, one obtains

$$\Phi = -\left[\cos^2\left(\frac{\theta}{2}\right) + \sin^2\left(\frac{\theta}{2}\right)\cos\gamma\right]n\Phi_0, \tag{43}$$

and if instead $\Delta\phi_2 = \Delta\phi_s = 2n\pi$ and $\Delta\phi_1 + \Delta\phi_2 = 0$, the flux is

$$\Phi = -\left[\cos^2\left(\frac{\theta}{2}\right) - \sin^2\left(\frac{\theta}{2}\right)\cos\gamma\right]n\Phi_0. \tag{44}$$

In either case, vortices can carry arbitrary fractional magnetic flux quanta.

More generally, for $\Delta\phi_s = 2k_s\pi$, $\Delta\phi_1 = 2k_1\pi$, and $\Delta\phi_2 = 2k_2\pi$, the flux carried by the vortex is given by:

$$|\Phi| = \lambda_{k_sk_1k_2}\Phi_0, \tag{45}$$

in which

$$\lambda_{k_sk_1k_2} = k_s\cos^2\left(\frac{\theta}{2}\right) + k_1\sin^2\left(\frac{\theta}{2}\right)\cos^2\left(\frac{\gamma}{2}\right) + k_2\sin^2\left(\frac{\theta}{2}\right)\sin^2\left(\frac{\gamma}{2}\right), \tag{46}$$

or alternatively

$$\lambda_{k_sk_1k_2} = \left(k_s\frac{|\psi_s|^2}{m_s} + k_1\frac{|\psi_1|^2}{m_1} + k_2\frac{|\psi_2|^2}{m_2}\right)\cdot\left(\frac{|\psi_s|^2}{m_s} + \frac{|\psi_1|^2}{m_1} + \frac{|\psi_2|^2}{m_2}\right)^{-1}, \tag{47}$$

which is again a fractional vortex with an arbitrary value of magnetic flux.

VI. CONCLUSIONS

In conclusion, we have investigated the existence of chiral topological superconductivity on a two-dimensional honeycomb lattice with tri-component-pairing gap function of mixed s-, $d_{x^-y^2}$-, and d_{xy}-wave symmetries. Using a Ginzburg-Landau free energy analysis, the overall pairing gap function can be determined as $s + d_{x^2-y^2}e^{i\phi_1} + d_{xy}e^{i\phi_2}$, which spontaneously breaks the time reversal, rotational, and reflectional symmetries. The symmetry-breaking pattern of the pairing configuration is $C_{6v}\times\mathbb{Z}_2^T \to C_2$, leading to 12 degenerate solutions of the ground state pairing configuration. Based on a microscopic model for the tri-component-pairing on the honeycomb lattice, the system is shown to be a fully gapped topological superconductor with nonzero Chern number and mid-gap edge states. Furthermore, the anomalous ac Hall conductivity is calculated to be non-vanishing, which breaks the C_6 rotational symmetry, reflecting the anisotropic nature of the tri-component-pairing gap function. Fractional vortices are also discussed, which arise from the multicomponent pairing structure of the system.

ACKNOWLEDGMENTS

Y.-H.L., J.J., and W.Y. are supported by the Fundamental Research Funds for the Central Universities. X.-X.Z. acknowledges the startup funding of Huazhong University of Science and Technology. C.W. is supported by the National Natural Science Foundation of China under the Grants No. 12234016 and No. 12174317. This work has been supported by the New Cornerstone Science Foundation.

DATA AVAILABILITY

The data that support the findings of this article are not publicly available upon publication because it is not technically feasible and/or the cost of preparing, depositing, and hosting the data would be prohibitive within the terms of this research project. The data are available from the authors upon reasonable request.

APPENDIX A: G-L FREE ENERGY ANALYSIS OF A TRI-COMPONENT PAIRING FUNCTION WITH C_{6v} SYMMETRY

In this section, we give a quick review of the C_{6v} group and G-L free energy. Here (x^2-y^2, xy) is an E_2 representation of the C_{6v} group, and A_1 representation is symmetric under all operations. The product rules for the A_1-, A_2-, and E_2-representations of C_{6v} and the corresponding example functions can be worked out as Table II:

The two generators of the C_{6v} group are $r = C_6$, and $f = l_1$, as defined in the main text. The generator relation representation for C_{6v} is $C_{6v} = \langle r, f | r^6 = f^2 = (rf)^6 = e\rangle$. Write $d_1 = \hat{d}_{x^2-y^2}$, and $d_2 = \hat{d}_{xy}$. The result of the action of the two group generators on this set of coordinates is

$$C_6\begin{pmatrix}d_1\\d_2\end{pmatrix} = \begin{pmatrix}-1/2 & \sqrt{3}/2\\ -\sqrt{3}/2 & -1/2\end{pmatrix}\begin{pmatrix}d_1\\d_2\end{pmatrix},$$
$$l_1\begin{pmatrix}d_1\\d_2\end{pmatrix} = \begin{pmatrix}1 & 0\\ 0 & -1\end{pmatrix}\begin{pmatrix}d_1\\d_2\end{pmatrix}. \tag{A1}$$

Since the coordinate of the linear term of d is (d_1, d_2), when we come to the quadratic term of d, A_1 is represented as $|d_1|^2 + |d_2|^2$, A_2 is represented as $i(d_1^*d_2 - d_2^*d_1)$, and E is represented as $(|d_1|^2 - |d_2|^2, d_1^*d_2 + d_2^*d_1)$.

1. Quadratic terms in free energy of d-wave

(d_1, d_2) forms an E_2-representation of C_{6v} group, and $E_2 \times E_2 = A_1 + A_2 + E_2$, there is only one C_{6v}-invariant combination, A_1. Thus we have only one term in the free energy of

TABLE II. Multiplication table of irreducible representations of the C_{6v} group.

C_{6v}	A_1	A_2	E_2	Functions
A_1	A_1	A_2	E_2	z, x^2+y^2, z^2
A_2		A_1	E_2	J_z
E_2			$A_1+A_2+E_2$	(x^2-y^2, xy)

d-wave up to quadratic level, i.e.,

$$f^{(2)} = |\psi_1|^2 + |\psi_2|^2. \tag{A2}$$

2. Cubic terms in free energy of d-wave

Although the free energy only contains even-order terms of the order parameters, the presence of an isotropic s-wave order parameter, in addition to the d-wave order parameters, allows the d-wave component to take cubic terms. These cubic terms, together with the first-order terms of the s-wave order parameter, contribute to the quartic terms in the free energy.

$$E_2 \times E_2 \times E_2 = (A_1 + A_2 + E_2) \times E_2, \tag{A3}$$

where the first E_2 on the right-hand side of Eq. (A3) is the quadratic term of d-wave components, and the second E_2 is the linear term.

The action of C_6 and l_1 on the E_2-representation which describes the linear term of the d-wave components is given by Eq. (A1), while the transformations of the E_2-representation which describes the quadratic term of the d-wave components are given by

$$C_6\begin{pmatrix}|d_1|^2-|d_2|^2\\ d_1^*d_2+d_2^*d_1\end{pmatrix} = \begin{pmatrix}-1/2 & -\sqrt{3}/2\\ \sqrt{3}/2 & -1/2\end{pmatrix}\begin{pmatrix}|d_1|^2-|d_2|^2\\ d_1^*d_2+d_2^*d_1\end{pmatrix},$$
$$l_1\begin{pmatrix}|d_1|^2-|d_2|^2\\ d_1^*d_2+d_2^*d_1\end{pmatrix} = \begin{pmatrix}1 & 0\\ 0 & -1\end{pmatrix}\begin{pmatrix}|d_1|^2-|d_2|^2\\ d_1^*d_2+d_2^*d_1\end{pmatrix}. \tag{A4}$$

It is evident that $(d_1, d_2)\sigma_z$ transforms in the same way as $(|d_1|^2 - |d_2|^2, d_1^*d_2 + d_2^*d_1)$ under the C_{6v} group, where σ_z is the Pauli matrix. Thus, there is one cubic term of d-wave order parameters,

$$f^{(3)} = \psi_1(|\psi_1|^2 - |\psi_2|^2) - \psi_2(\psi_1^*\psi_2 + \psi_2^*\psi_1). \tag{A5}$$

3. Quartic terms in free energy of d-wave

Up to quartic terms, we need to consider the product $(E_2 \times E_2) \times (E_2 \times E_2)$,

$$\begin{aligned}&(E_2 \times E_2) \times (E_2 \times E_2)\\ &= (A_1 + A_2 + E_2) \times (A_1 + A_2 + E_2)\\ &= A_1 + A_2 + E_2 + A_2 + A_1 + E_2 + E_2\\ &\quad + E_2 + (A_1 + A_2 + E_2).\end{aligned} \tag{A6}$$

So there should be three extra C_{6v}-invariant terms in the free energy up to quartic terms:

$$\begin{aligned}&A_1 \times A_1 : f_1^{(4)} = (|\psi_1|^2 + |\psi_2|^2)^2,\\ &A_2 \times A_2 : f_2^{(4)} = -(\psi_1^*\psi_2 - \psi_2^*\psi_1)^2,\\ &E_2 \times E_2 : f_3^{(4)} = (|\psi_1|^2 - |\psi_2|^2)^2 + (\psi_1^*\psi_2 + \psi_2^*\psi_1)^2.\end{aligned} \tag{A7}$$

However, $f_3^{(4)} = |\psi_1|^4 + |\psi_2|^4 + \psi_1^{*2}\psi_2^2 + \psi_2^{*2}\psi_1^2 = f_1^{(4)} - f_2^{(4)}$, thus, there are only two extra linearly independent terms up to quartic level.

If we include the mixture with an s-wave pairing order parameter, the overall free energy up to the quartic order is

$$\begin{aligned}F = {}&\alpha_d(|\psi_1|^2 + |\psi_2|^2) + \beta_d(|\psi_1|^2 + |\psi_2|^2)^2\\ &+ \alpha_s|\psi_s|^2 + \beta_s|\psi_s|^4 + \gamma|\psi_s|^2(|\psi_1|^2 + |\psi_2|^2)\\ &+ g_{dd}(\psi_1^*\psi_2 - \psi_1\psi_2^*)^2\\ &+ g_{sd}\left[\psi_s^2\left(\psi_1^{*2} + \psi_2^{*2}\right) + \psi_s^{*2}\left(\psi_1^2 + \psi_2^2\right)\right]\\ &+ g'_{sd}[(\psi_s^*\psi_1 + \psi_s\psi_1^*)(|\psi_1|^2 - |\psi_2|^2)\\ &- (\psi_s^*\psi_2 + \psi_s\psi_2^*)(\psi_1^*\psi_2 + \psi_1\psi_2^*)].\end{aligned} \tag{A8}$$

APPENDIX B: d-WAVE SYMMETRY OF THE PAIRING FUNCTIONS $\Delta_{x^2-y^2}$ AND Δ_{xy}

For simplicity, the pairing term involving $\Delta_{x^2-y^2}$ and Δ_{xy} separately can be considered as

$$\Delta_d(\boldsymbol{k}) = \Delta_{x^2-y^2}(\boldsymbol{k})e^{i\phi_1} + \Delta_{xy}(\boldsymbol{k})e^{i\phi_2}, \tag{B1}$$

where the definitions of $\Delta_{x^2-y^2}$ and Δ_{xy} are given in Eq. (17) in the main text. Let

$$\begin{aligned}g_1 &= |\psi_1|e^{i\phi_1}\left[\cos(k_x a) - \cos\left(\frac{1}{2}k_x a\right)\cos\left(\frac{\sqrt{3}}{2}k_y a\right)\right],\\ g_2 &= |\psi_2|e^{i\phi_2}\left[-\sqrt{3}\sin\left(\frac{1}{2}k_x a\right)\sin\left(\frac{\sqrt{3}}{2}k_y a\right)\right],\\ -h_1 &= -|\psi_1|e^{i\phi_1}\left[\sin(k_x a) + \sin\left(\frac{1}{2}k_x a\right)\cos\left(\frac{\sqrt{3}}{2}k_y a\right)\right],\\ h_2 &= |\psi_2|e^{i\phi_2}\left[\sqrt{3}\cos\left(\frac{1}{2}k_x a\right)\sin\left(\frac{\sqrt{3}}{2}k_y a\right)\right].\end{aligned} \tag{B2}$$

In this case, we have

$$\begin{aligned}\Delta_{x^2-y^2}(\boldsymbol{k})e^{i\phi_1} &= g_1\sigma_x + (-h_1)\sigma_y,\\ \Delta_{xy}(\boldsymbol{k})e^{i\phi_2} &= g_2\sigma_x + h_2\sigma_y.\end{aligned} \tag{B3}$$

The pairing operator that only involves $\Delta_{x^2-y^2}$ and Δ_{xy} can be written as

$$\hat{\Delta}_d = \sum_{\boldsymbol{k}} \Psi_{\boldsymbol{k}}^\dagger \begin{pmatrix}0 & \Delta_d(\boldsymbol{k})\\ \Delta_d^\dagger(\boldsymbol{k}) & 0\end{pmatrix}\Psi_{\boldsymbol{k}}, \tag{B4}$$

or more explicitly,

$$\hat{\Delta}_d = \sum_{\boldsymbol{k}} (c^\dagger_{\boldsymbol{k}_A}\, c^\dagger_{\boldsymbol{k}_B}\, c_{-\boldsymbol{k}_A}\, c_{-\boldsymbol{k}_B}) \begin{pmatrix} 0 & (g_1+g_2)\sigma_x + (-h_1+h_2)\sigma_y \\ [(g_1+g_2)\sigma_x + (-h_1+h_2)\sigma_y]^\dagger & 0 \end{pmatrix} \begin{pmatrix} c_{\boldsymbol{k}_A} \\ c_{\boldsymbol{k}_B} \\ c^\dagger_{-\boldsymbol{k}_A} \\ c^\dagger_{-\boldsymbol{k}_B} \end{pmatrix}, \tag{B5}$$

where the spin indices are omitted because we focus on the momentum, with upward spin always paired with positive momentum and downward spin with negative momentum. Consider the two parts that include σ_x and σ_y separately,

$$\Delta_d(\boldsymbol{k}) = \Delta_{dx}(\boldsymbol{k}) + \Delta_{dy}(\boldsymbol{k}), \tag{B6}$$

in which $\Delta_{dx}(\boldsymbol{k}) = (g_1+g_2)\sigma_x$, and $\Delta_{dy}(\boldsymbol{k}) = (-h_1+h_2)\sigma_y$.

The action of C_6 rotation on $\hat{\Delta}_{dx}$ is

$$\begin{aligned} \hat{U}(C_6)\hat{\Delta}_{dx}\hat{U}^\dagger(C_6) &= \sum_{\boldsymbol{k}} \hat{U}(C_6)\Psi^\dagger_{\boldsymbol{k}}\hat{U}^\dagger(C_6)\hat{U}(C_6) \begin{pmatrix} 0 & (g_1+g_2)\sigma_x \\ [(g_1+g_2)\sigma_x]^\dagger & 0 \end{pmatrix} \hat{U}^\dagger(C_6)\hat{U}(C_6)\Psi_{\boldsymbol{k}}\hat{U}^\dagger(C_6) \\ &= \sum_{\boldsymbol{k}} (c^\dagger_{\boldsymbol{k}_A}\, c^\dagger_{\boldsymbol{k}_B}\, c_{-\boldsymbol{k}_A}\, c_{-\boldsymbol{k}_B}) \begin{pmatrix} 0 & (g_1'+g_2')\sigma_x \\ [(g_1'+g_2')\sigma_x]^\dagger & 0 \end{pmatrix} \begin{pmatrix} c_{\boldsymbol{k}_A} \\ c_{\boldsymbol{k}_B} \\ c^\dagger_{-\boldsymbol{k}_A} \\ c^\dagger_{-\boldsymbol{k}_B} \end{pmatrix}, \end{aligned} \tag{B7}$$

in which

$$\begin{aligned} g_1' &= |\psi_1|e^{i\phi_1}\left\{-\frac{1}{2}\left[\cos(k_x a) - \cos\left(\frac{1}{2}k_x a\right)\cos\left(\frac{\sqrt{3}}{2}k_y a\right)\right] - \frac{\sqrt{3}}{2}\left[-\sqrt{3}\sin\left(\frac{1}{2}k_x a\right)\sin\left(\frac{\sqrt{3}}{2}k_y a\right)\right]\right\}, \\ g_2' &= |\psi_2|e^{i\phi_2}\left\{\frac{\sqrt{3}}{2}\left[\cos(k_x a) - \cos\left(\frac{1}{2}k_x a\right)\cos\left(\frac{\sqrt{3}}{2}k_y a\right)\right] - \frac{1}{2}\left[-\sqrt{3}\sin\left(\frac{1}{2}k_x a\right)\sin\left(\frac{\sqrt{3}}{2}k_y a\right)\right]\right\}. \end{aligned} \tag{B8}$$

The action of the l_1 mirror reflection on $\hat{\Delta}_{dx}$ is

$$\begin{aligned} \hat{U}(l_1)\hat{\Delta}_{dx}\hat{U}^\dagger(l_1) &= \sum_{\boldsymbol{k}} \hat{U}(l_1)\Psi^\dagger_{\boldsymbol{k}}\hat{U}^\dagger(l_1)\hat{U}(l_1) \begin{pmatrix} 0 & (g_1+g_2)\sigma_x \\ [(g_1+g_2)\sigma_x]^\dagger & 0 \end{pmatrix} \hat{U}^\dagger(l_1)\hat{U}(l_1)\Psi_{\boldsymbol{k}}\hat{U}^\dagger(l_1) \\ &= \sum_{\boldsymbol{k}} (c^\dagger_{\boldsymbol{k}_A}\, c^\dagger_{\boldsymbol{k}_B}\, c_{-\boldsymbol{k}_A}\, c_{-\boldsymbol{k}_B}) \begin{pmatrix} 0 & (g_1''+g_2'')\sigma_x \\ [(g_1''+g_2'')\sigma_x]^\dagger & 0 \end{pmatrix} \begin{pmatrix} c_{\boldsymbol{k}_A} \\ c_{\boldsymbol{k}_B} \\ c^\dagger_{-\boldsymbol{k}_A} \\ c^\dagger_{-\boldsymbol{k}_B} \end{pmatrix}, \end{aligned} \tag{B9}$$

where

$$\begin{aligned} g_1'' &= |\psi_1|e^{i\phi_1}\left[\cos(k_x a) - \cos\left(\frac{1}{2}k_x a\right)\cos\left(-\frac{\sqrt{3}}{2}k_y a\right)\right] = g_1, \\ g_2'' &= |\psi_2|e^{i\phi_2}\left[-\sqrt{3}\sin\left(\frac{1}{2}k_x a\right)\sin\left(-\frac{\sqrt{3}}{2}k_y a\right)\right] = -g_2. \end{aligned} \tag{B10}$$

Thus, $(g_1\sigma_x, g_2\sigma_x)$ forms an E_2 representation of the C_{6v} group.

On the other hand, the action of C_6 rotation on $\hat{\Delta}_{dy}$ is

$$\begin{aligned} \hat{U}(C_6)\hat{\Delta}_{dy}\hat{U}^\dagger(C_6) &= \sum_{\boldsymbol{k}} \hat{U}(C_6)\Psi^\dagger_{\boldsymbol{k}}\hat{U}^\dagger(C_6)\hat{U}(C_6) \begin{pmatrix} 0 & (-h_1+h_2)\sigma_y \\ [(-h_1+h_2)\sigma_y]^\dagger & 0 \end{pmatrix} \hat{U}^\dagger(C_6)\hat{U}(C_6)\Psi_{\boldsymbol{k}}\hat{U}^\dagger(C_6) \\ &= \sum_{\boldsymbol{k}} (c^\dagger_{\boldsymbol{k}_A}\, c^\dagger_{\boldsymbol{k}_B}\, c_{-\boldsymbol{k}_A}\, c_{-\boldsymbol{k}_B}) \begin{pmatrix} 0 & (-h_1'+h_2')\sigma_y \\ [(-h_1'+h_2')\sigma_y]^\dagger & 0 \end{pmatrix} \begin{pmatrix} c_{\boldsymbol{k}_A} \\ c_{\boldsymbol{k}_B} \\ c^\dagger_{-\boldsymbol{k}_A} \\ c^\dagger_{-\boldsymbol{k}_B} \end{pmatrix}, \end{aligned} \tag{B11}$$

in which

$$\begin{aligned} -h_1' &= -|\psi_1|e^{i\phi_1}\left\{-\frac{1}{2}\left[\sin(k_x a) + \sin\left(\frac{1}{2}k_x a\right)\cos\left(\frac{\sqrt{3}}{2}k_y a\right)\right] + \frac{\sqrt{3}}{2}\left[\sqrt{3}\cos\left(\frac{1}{2}k_x a\right)\sin\left(\frac{\sqrt{3}}{2}k_y a\right)\right]\right\}, \\ h_2' &= |\psi_2|e^{i\phi_2}\left\{-\frac{\sqrt{3}}{2}\left[\sin(k_x a) + \sin\left(\frac{1}{2}k_x a\right)\cos\left(\frac{\sqrt{3}}{2}k_y a\right)\right] - \frac{1}{2}\left[\sqrt{3}\cos\left(\frac{1}{2}k_x a\right)\sin\left(\frac{\sqrt{3}}{2}k_y a\right)\right]\right\}. \end{aligned} \tag{B12}$$

The result of the l_1 mirror reflection acting on $\hat{\Delta}_{dy}$ is

$$\begin{aligned}\hat{U}(l_1)\hat{\Delta}_{dy}\hat{U}^\dagger(l_1) &= \sum_{\boldsymbol{k}} \hat{U}(l_1)\Psi^\dagger_{\boldsymbol{k}}\hat{U}^\dagger(l_1)\hat{U}(l_1)\begin{pmatrix} 0 & (-h_1+h_2)\sigma_y \\ [(-h_1+h_2)\sigma_y]^\dagger & 0\end{pmatrix}\hat{U}^\dagger(l_1)\hat{U}(l_1)\Psi_{\boldsymbol{k}}\hat{U}^\dagger(l_1)\\ &= \sum_{\boldsymbol{k}}(c^\dagger_{\boldsymbol{k}_A}\ c^\dagger_{\boldsymbol{k}_B}\ c_{-\boldsymbol{k}_A}\ c_{-\boldsymbol{k}_B})\begin{pmatrix} 0 & (-h_1''+h_2'')\sigma_y \\ [(-h_1''+h_2'')\sigma_y]^\dagger & 0\end{pmatrix}\begin{pmatrix} c_{\boldsymbol{k}_A}\\ c_{\boldsymbol{k}_B}\\ c^\dagger_{-\boldsymbol{k}_A}\\ c^\dagger_{-\boldsymbol{k}_B}\end{pmatrix},\end{aligned} \tag{B13}$$

where

$$\begin{aligned}-h_1'' &= -|\psi_1|e^{i\phi_1}\left[\sin(k_x''a)+\sin\left(\frac{1}{2}k_x''a\right)\cos\left(-\frac{\sqrt{3}}{2}k_y''a\right)\right]=-h_1,\\ h_2'' &= |\psi_2|e^{i\phi_2}\left[\sqrt{3}\cos\left(\frac{1}{2}k_x''a\right)\sin\left(-\frac{\sqrt{3}}{2}k_y''a\right)\right]=-h_2.\end{aligned} \tag{B14}$$

Therefore, $(-h_1\sigma_y, h_2\sigma_y)$ also forms an E_2 representation of the C_{6v} group.

Since $(\Delta_{x^2-y^2}, \Delta_{xy})$ is a linear combination of $(g_1\sigma_x, g_2\sigma_x)$ and $(-h_1\sigma_y, h_2\sigma_y)$, $(\Delta_{x^2-y^2}, \Delta_{xy})$ is also an E_2 representation of the C_{6v} group and thus transforms in the same way as $(d_{x^2-y^2}, d_{xy})$.

APPENDIX C: ANOMALOUS ac HALL CONDUCTIVITY UNDER THE MIRROR REFLECTION SYMMETRIES OF C_{6v}

From Eq. (29) in the main text, the current-current correlator is

$$\pi_{xy}(\boldsymbol{q},\omega) = \int_0^\infty dt e^{i\omega t}\langle[\hat{J}^\dagger_x(\boldsymbol{q},t),\hat{J}_y(\boldsymbol{q},0)]\rangle, \tag{C1}$$

where $\hat{J}_\alpha = e\sum_{\boldsymbol{k}}\Psi^\dagger_{\boldsymbol{k}}\hat{v}_\alpha\Psi_{\boldsymbol{k}}$, and $\hat{v}_\alpha = (\sigma_z\otimes\sigma_0)(1/\hbar)\partial_{k_\alpha}h^0_{\boldsymbol{k}}$, $\alpha = x, y$, i.e,

$$\hat{v}_\alpha = \begin{pmatrix}1&0&0&0\\0&1&0&0\\0&0&-1&0\\0&0&0&-1\end{pmatrix}\frac{1}{\hbar}\partial_{k_\alpha}\begin{pmatrix}-\mu & \epsilon_x-i\epsilon_y & 0 & 0\\ \epsilon_x+i\epsilon_y & -\mu & 0 & 0\\ 0&0&\mu&-\epsilon_x+i\epsilon_y\\ 0&0&-\epsilon_x-i\epsilon_y&\mu\end{pmatrix} = \begin{pmatrix}0&v_\alpha&0&0\\ v^*_\alpha&0&0&0\\0&0&0&v_\alpha\\0&0&v^*_\alpha&0\end{pmatrix}, \tag{C2}$$

in which $v_\alpha = (1/\hbar)\partial_{k_\alpha}(\epsilon_x - i\epsilon_y)$, $v^*_\alpha = (1/\hbar)\partial_{k_\alpha}(\epsilon_x+i\epsilon_y)$. For v_x and v_y,

$$\begin{aligned}\partial_{k_x}\epsilon_x &= ta\left[\sin(k_xa)+\frac{1}{2}\sin\left(\frac{1}{2}k_xa-\frac{\sqrt{3}}{2}k_ya\right)+\frac{1}{2}\sin\left(\frac{1}{2}k_xa+\frac{\sqrt{3}}{2}k_ya\right)\right],\\ \partial_{k_x}\epsilon_y &= ta\left[\cos(k_xa)-\frac{1}{2}\cos\left(\frac{1}{2}k_xa-\frac{\sqrt{3}}{2}k_ya\right)-\frac{1}{2}\cos\left(\frac{1}{2}k_xa+\frac{\sqrt{3}}{2}k_ya\right)\right],\\ \partial_{k_y}\epsilon_x &= -\frac{\sqrt{3}}{2}ta\left[\sin\left(\frac{1}{2}k_xa-\frac{\sqrt{3}}{2}k_ya\right)-\sin\left(\frac{1}{2}k_xa+\frac{\sqrt{3}}{2}k_ya\right)\right],\\ \partial_{k_y}\epsilon_y &= \frac{\sqrt{3}}{2}ta\left[\cos\left(\frac{1}{2}k_xa-\frac{\sqrt{3}}{2}k_ya\right)-\cos\left(\frac{1}{2}k_xa+\frac{\sqrt{3}}{2}k_ya\right)\right].\end{aligned} \tag{C3}$$

Under mirror reflection transformation along x axis, i.e, the l_1 reflection defined in Fig. 3 in the main text, the above partial derivatives transform as

$$\begin{aligned}l_1(\partial_{k_x}\epsilon_x) &= \partial_{k_x}\epsilon_x,\\ l_1(\partial_{k_x}\epsilon_y) &= \partial_{k_x}\epsilon_x,\\ l_1(\partial_{k_y}\epsilon_x) &= -\partial_{k_y}\epsilon_x,\\ l_1(\partial_{k_y}\epsilon_y) &= -\partial_{k_y}\epsilon_x.\end{aligned} \tag{C4}$$

Thus, $l_1 v_x = v_x$, $l_1 v_y = -v_y$, and then

$$l_1\hat{J}_x = e\sum_{\boldsymbol{k}}\left(c^\dagger_{\boldsymbol{k}_A}\ c^\dagger_{\boldsymbol{k}_B}\ c_{-\boldsymbol{k}_A}\ c_{-\boldsymbol{k}_B}\right)\begin{pmatrix}0 & v_x & 0 & 0\\ v_x^* & 0 & 0 & 0\\ 0 & 0 & 0 & v_x\\ 0 & 0 & v_x^* & 0\end{pmatrix}\begin{pmatrix}c_{\boldsymbol{k}_A}\\ c_{\boldsymbol{k}_B}\\ c^\dagger_{-\boldsymbol{k}_A}\\ c^\dagger_{-\boldsymbol{k}_B}\end{pmatrix} = \hat{J}_x,$$

$$l_1\hat{J}_y = e\sum_{\boldsymbol{k}}\left(c^\dagger_{\boldsymbol{k}_A}\ c^\dagger_{\boldsymbol{k}_B}\ c_{-\boldsymbol{k}_A}\ c_{-\boldsymbol{k}_B}\right)\begin{pmatrix}0 & -v_y & 0 & 0\\ -v_y^* & 0 & 0 & 0\\ 0 & 0 & 0 & -v_y\\ 0 & 0 & -v_y^* & 0\end{pmatrix}\begin{pmatrix}c_{\boldsymbol{k}_A}\\ c_{\boldsymbol{k}_B}\\ c^\dagger_{-\boldsymbol{k}_A}\\ c^\dagger_{-\boldsymbol{k}_B}\end{pmatrix} = -\hat{J}_y. \tag{C5}$$

Under mirror reflection transformation along y axis, i.e, the l_4 reflection defined in Fig. 3 in the main text, the above partial derivatives transform as

$$\begin{aligned} l_4\left(\partial_{k_x}\epsilon_x\right) &= -\partial_{k_x}\epsilon_x,\\ l_4\left(\partial_{k_x}\epsilon_y\right) &= \partial_{k_x}\epsilon_x,\\ l_4\left(\partial_{k_y}\epsilon_x\right) &= \partial_{k_y}\epsilon_x,\\ l_4\left(\partial_{k_y}\epsilon_y\right) &= -\partial_{k_y}\epsilon_x. \end{aligned} \tag{C6}$$

Thus $l_4 v_x = -v_x^*$, $l_4 v_y = v_y^*$, and

$$l_4\hat{J}_x = e\sum_{\boldsymbol{k}}\left(c^\dagger_{\boldsymbol{k}_B}\ c^\dagger_{\boldsymbol{k}_A}\ c_{-\boldsymbol{k}_B}\ c_{-\boldsymbol{k}_A}\right)\begin{pmatrix}0 & -v_x^* & 0 & 0\\ -v_x & 0 & 0 & 0\\ 0 & 0 & 0 & -v_x^*\\ 0 & 0 & -v_x & 0\end{pmatrix}\begin{pmatrix}c_{\boldsymbol{k}_B}\\ c_{\boldsymbol{k}_A}\\ c^\dagger_{-\boldsymbol{k}_B}\\ c^\dagger_{-\boldsymbol{k}_A}\end{pmatrix} = -\hat{J}_x,$$

$$l_4\hat{J}_y = e\sum_{\boldsymbol{k}}\left(c^\dagger_{\boldsymbol{k}_B}\ c^\dagger_{\boldsymbol{k}_A}\ c_{-\boldsymbol{k}_B}\ c_{-\boldsymbol{k}_A}\right)\begin{pmatrix}0 & v_y^* & 0 & 0\\ v_y & 0 & 0 & 0\\ 0 & 0 & 0 & v_y^*\\ 0 & 0 & v_y & 0\end{pmatrix}\begin{pmatrix}c_{\boldsymbol{k}_B}\\ c_{\boldsymbol{k}_A}\\ c^\dagger_{-\boldsymbol{k}_B}\\ c^\dagger_{-\boldsymbol{k}_A}\end{pmatrix} = \hat{J}_y. \tag{C7}$$

Therefore $l_1\pi_{xy}(\boldsymbol{q},\omega) = -\pi_{xy}(\boldsymbol{q},\omega)$, $l_4\pi_{xy}(\boldsymbol{q},\omega) = -\pi_{xy}(\boldsymbol{q},\omega)$, meaning that under mirror reflection transformation along $\hat{x}$ or $\hat{y}$ axis, the current correlator changes as $\pi_{xy} \to -\pi_{xy}$, which results in a sign change of σ_H.

However, if the mirror symmetry axis is not aligned with the $\hat{x}$ or $\hat{y}$ axis, but instead coincides with one of the other four axes defined in Fig. 3 of the main text (e.g., the l_2-reflection), the transformation of the aforementioned partial derivatives becomes

$$\begin{aligned} l_2\left(\partial_{k_x}\epsilon_x\right) &= ta\left[\sin\left(\frac{1}{2}k_x a + \frac{\sqrt{3}}{2}k_y a\right) - \frac{1}{2}\sin\left(\frac{1}{2}k_x a - \frac{\sqrt{3}}{2}k_y a\right) + \frac{1}{2}\sin\left(k_x a\right)\right],\\ l_2\left(\partial_{k_x}\epsilon_y\right) &= ta\left[\cos\left(\frac{1}{2}k_x a + \frac{\sqrt{3}}{2}k_y a\right) - \frac{1}{2}\cos\left(\frac{1}{2}k_x a - \frac{\sqrt{3}}{2}k_y a\right) - \frac{1}{2}\cos\left(k_x a\right)\right],\\ l_2\left(\partial_{k_y}\epsilon_x\right) &= -\frac{\sqrt{3}}{2}ta\left[-\sin\left(\frac{1}{2}k_x a - \frac{\sqrt{3}}{2}k_y a\right) - \sin\left(k_x a\right)\right],\\ l_2\left(\partial_{k_y}\epsilon_y\right) &= \frac{\sqrt{3}}{2}ta\left[\cos\left(\frac{1}{2}k_x a - \frac{\sqrt{3}}{2}k_y a\right) - \cos\left(k_x a\right)\right]. \end{aligned} \tag{C8}$$

And the transformations under l_3, l_5, and l_6 reflections follow analogously. Consequently, within the C_{6v} point group, the four mirror reflection operations other than those along the $\hat{x}$ and $\hat{y}$ axes do not enforce a sign reversal of σ_H. Therefore a nonzero anomalous ac Hall conductivity can be realized without breaking the l_2-, l_3-, l_5-, and l_6-reflection symmetries.

APPENDIX D: ANOMALOUS ac HALL CONDUCTIVITY FORMULAS

Perform an S-matrix expansion of the current-current correlator, Eq. (29), to one-loop level, we have

$$\pi_{xy}(\boldsymbol{q},\nu_m) = \frac{ie^2}{\beta}\sum_{\boldsymbol{k},\omega_n}\mathrm{Tr}\left[\hat{v}_x\left(\boldsymbol{k}+\frac{\boldsymbol{q}}{2}\right)G_0(\boldsymbol{k},\omega_n)\hat{v}_y\left(\boldsymbol{k}+\frac{\boldsymbol{q}}{2}\right)G_0(\boldsymbol{k}+\boldsymbol{q},\omega_n+\nu_m)\right], \tag{D1}$$

where $G_0(\boldsymbol{k},\omega_n)=(i\hbar\omega_n-h_{\boldsymbol{k}})^{-1}$, and ω_n is the fermionic Matsubara frequency, satisfying $\hbar\omega_n=(2n+1)\pi/\beta$. Take the antisymmetric difference of (D1) and simplify for the $\boldsymbol{q}=0$ case of interest,

$$\pi_{xy}(\nu_m)-\pi_{yx}(\nu_m)=\frac{ie^2}{\beta}\sum_{\boldsymbol{k},\omega_n}\frac{4\hbar\nu_m(\hbar\nu_m+2\hbar\omega_n)^2(v_x^*v_y-v_xv_y^*)[\mu(\Delta_x^*\Delta_y-\Delta_x\Delta_y^*)+2i\Delta_s(\epsilon_x\mathrm{Im}\Delta_y-\epsilon_y\mathrm{Im}\Delta_x)]}{\left(\hbar^2\omega_n^2+E_1^2\right)\left(\hbar^2\omega_n^2+E_2^2\right)\left[\hbar^2(\omega_n+\nu_m)^2+E_1^2\right]\left[\hbar^2(\omega_n+\nu_m)^2+E_2^2\right]}, \tag{D2}$$

Thus the anomalous ac Hall conductivity can be written as

$$\begin{aligned}\sigma_H(\nu_m)&=\frac{1}{2\hbar\omega}[\pi_{xy}(\nu_m)-\pi_{yx}(\nu_m)]\\&=\frac{e^2}{\hbar\beta}\int\frac{d^2k}{(2\pi)^2}\sum_{\omega_n}\frac{2\hbar(\hbar\nu_m+2\hbar\omega_n)^2(v_x^*v_y-v_xv_y^*)[\mu(\Delta_x^*\Delta_y-\Delta_x\Delta_y^*)+2i\Delta_s(\epsilon_x\mathrm{Im}\Delta_y-\epsilon_y\mathrm{Im}\Delta_x)]}{\left(\hbar^2\omega_n^2+E_1^2\right)\left(\hbar^2\omega_n^2+E_2^2\right)\left[\hbar^2(\omega_n+\nu_m)^2+E_1^2\right]\left[\hbar^2(\omega_n+\nu_m)^2+E_2^2\right]}.\end{aligned} \tag{D3}$$

Taking the limit $i\nu_m\to\omega+i\epsilon$, the above equation corresponds to Eq. (32) in the main text. By performing the Matsubara summation over ω_n, we obtain

$$\begin{aligned}\sigma_H(\omega)=\frac{e^2}{\hbar}\int\frac{d^2k}{(2\pi)^2}&\hbar^2(v_x^*v_y-v_xv_y^*)[\mu(\Delta_x^*\Delta_y-\Delta_x\Delta_y^*)+2i\Delta_s(\epsilon_x\mathrm{Im}\Delta_y-\epsilon_y\mathrm{Im}\Delta_x)]\\&\times\left\{\frac{1-n_F(E_1)-n_F(E_2)}{2E_1E_2(E_1+E_2)^2}\left[\frac{E_1+E_2+\hbar\omega-i\epsilon}{(E_1+E_2+\hbar\omega)^2+\epsilon^2}+\frac{E_1+E_2-\hbar\omega+i\epsilon}{(E_1+E_2-\hbar\omega)^2+\epsilon^2}\right]\right.\\&\left.-\frac{n_F(E_1)-n_F(E_2)}{2E_1E_2(E_1-E_2)^2}\left[\frac{E_1-E_2+\hbar\omega-i\epsilon}{(E_1-E_2+\hbar\omega)^2+\epsilon^2}+\frac{E_1-E_2-\hbar\omega+i\epsilon}{(E_1-E_2-\hbar\omega)^2+\epsilon^2}\right]\right\},\end{aligned} \tag{D4}$$

where ϵ is a positive infinitesimal. At $T=0\,\mathrm{K}$, $n_F(E_1)=n_F(E_2)=0$, and $[\sigma_H(\omega)]_{T=0\,\mathrm{K}}$ can be written as

$$\begin{aligned}[\sigma_H(\omega)]_{T=0\,\mathrm{K}}=\frac{e^2}{\hbar}\int\frac{d^2k}{(2\pi)^2}&\hbar^2(v_x^*v_y-v_xv_y^*)[\mu(\Delta_x^*\Delta_y-\Delta_x\Delta_y^*)+2i\Delta_s(\epsilon_x\mathrm{Im}\Delta_y-\epsilon_y\mathrm{Im}\Delta_x)]\\&\times\frac{1}{2E_1E_2(E_1+E_2)^2}\left[\frac{E_1+E_2+\hbar\omega-i\epsilon}{(E_1+E_2+\hbar\omega)^2+\epsilon^2}+\frac{E_1+E_2-\hbar\omega+i\epsilon}{(E_1+E_2-\hbar\omega)^2+\epsilon^2}\right].\end{aligned} \tag{D5}$$

APPENDIX E: SUPERCURRENT OF THE TRI-COMPONENT-PAIRING SUPERCONDUCTOR IN MAGNETIC FIELDS

It is not straightforward to infer the vortex configurations directly from Eq. (36) in the main text. As pointed out in Ref. [82], the GL free energy functional of a two-gap superconductor can be exactly mapped onto the extended Faddeev model, which consists of a three-component unit vector $\boldsymbol{n}$, a massive vector field $\mathbf{C}$, and a density-related variable ρ. In the tri-component superconducting system with $d_{x^2-y^2}$-, d_{xy}-, and s-wave pairings, $\boldsymbol{n}$ is extended to an eight-component vector in the $SU(3)$ case, defined in terms of the normalized complex order-parameter vector z and the $SU(3)$ Gell-Mann matrices $\lambda_a(a=1,2,\ldots,8)$:

$$n_a=z^\dagger\lambda_a z, \tag{E1}$$

in which

$$z=\frac{1}{\rho}\left(\frac{\psi_s}{\sqrt{2m_s}}\ \frac{\psi_1}{\sqrt{2m_1}}\ \frac{\psi_2}{\sqrt{2m_2}}\right)^T, \tag{E2}$$

and the order parameters can be written as

$$\begin{aligned}\psi_s&=\sqrt{2m_s}\rho\cos\left(\frac{\theta}{2}\right)e^{i\phi_s},\\\psi_1&=\sqrt{2m_1}\rho\sin\left(\frac{\theta}{2}\right)\cos\left(\frac{\gamma}{2}\right)e^{i\phi_1},\\\psi_2&=\sqrt{2m_2}\rho\sin\left(\frac{\theta}{2}\right)\sin\left(\frac{\gamma}{2}\right)e^{i\phi_2}.\end{aligned} \tag{E3}$$

Substituting Eq. (E3) into Eq. (36) and adopting the London limit ($|\psi_{s,1,2}|=\mathrm{const}$), we obtain

$$F=\frac{\rho^2}{4}\sum_a(\nabla n_a)^2+\frac{\rho^2}{16}\mathbf{C}^2+\frac{\mathbf{B}^2}{2}+V_0+V_{\rho Kn}, \tag{E4}$$

where

$$\mathbf{C} = \frac{i}{m_s\rho^2}(\psi_s^*\nabla\psi_s - \psi_s\nabla\psi_s^*) + \frac{i}{m_1\rho^2}(\psi_1^*\nabla\psi_1 - \psi_1\nabla\psi_1^*) + \frac{i}{m_2\rho^2}(\psi_2^*\nabla\psi_2 - \psi_2\nabla\psi_2^*) - \frac{4e}{\rho^2}\left(\frac{|\psi_s|^2}{m_s} + \frac{|\psi_1|^2}{m_1} + \frac{|\psi_2|^2}{m_2}\right)\mathbf{A}, \tag{E5}$$

$$V_0 = F_s^{(0)} + F_d^{(0)} - 2g_{dd}|\psi_1|^2|\psi_2|^2, \tag{E6}$$

and

$$V_{\rho Kn} = \rho^4\left[K_1\left(n_1^2 - n_2^2\right) + K_2\left(n_4^2 - n_5^2\right) + K_3\left(n_6^2 - n_7^2\right) + K_4 n_1 n_3' + K_5 n_4 n_6\right], \tag{E7}$$

in which $K_1 = 2g_{sd}m_s m_1$, $K_2 = 2g_{sd}m_s m_2$, $K_3 = 2g_{dd}m_1 m_2$, $K_4 = 4g'_{sd}\sqrt{m_s m_1}$, $K_5 = 4g'_{sd}m_2\sqrt{m_s m_1}$, and

$$\begin{aligned}
&n_1 = \sin\theta\cos\left(\frac{\gamma}{2}\right)\cos\delta_1,\ n_2 = \sin\theta\cos\left(\frac{\gamma}{2}\right)\sin\delta_1,\\
&n_3 = \sin^2\left(\frac{\theta}{2}\right)\cos\gamma,\ n_3' = \sin^2\left(\frac{\theta}{2}\right)\left[m_1\cos^2\left(\frac{\gamma}{2}\right) - m_2\sin^2\left(\frac{\gamma}{2}\right)\right],\\
&n_4 = \sin\theta\sin\left(\frac{\gamma}{2}\right)\cos\delta_2,\ n_5 = \sin\theta\sin\left(\frac{\gamma}{2}\right)\sin\delta_2,\\
&n_6 = \sin^2\left(\frac{\theta}{2}\right)\sin\gamma\cos\delta_0,\ n_7 = \sin^2\left(\frac{\theta}{2}\right)\sin\gamma\sin\delta_0,\\
&n_8 = \frac{1}{\sqrt{3}}\left[\cos^2\left(\frac{\theta}{2}\right) + \sin^2\left(\frac{\theta}{2}\right)\cos^2\left(\frac{\gamma}{2}\right) - 2\sin^2\left(\frac{\theta}{2}\right)\cos^2\left(\frac{\gamma}{2}\right)\right],
\end{aligned} \tag{E8}$$

where $\gamma_{0,1,2}$ denote the relative phase differences among the three order parameters, with $\gamma_0 = \phi_1 - \phi_2$, $\gamma_1 = \phi_1 - \phi_s$, and $\gamma_2 = \phi_2 - \phi_s$. The free energy functional can be further expressed as:

$$\begin{aligned}
F = {}& \frac{\rho^2}{4}\left[\sin^2\theta\cos^2\left(\frac{\gamma}{2}\right)(\nabla\gamma_1)^2 + \sin^2\theta\sin^2\left(\frac{\gamma}{2}\right)(\nabla\gamma_2)^2 + \sin^4\left(\frac{\theta}{2}\right)\sin^2\gamma(\nabla\gamma_0)^2\right]\\
&+ \rho^2\left[\sin^2\left(\frac{\theta}{2}\right)\cos^2\left(\frac{\gamma}{2}\right)\nabla\phi_1 + \sin^2\left(\frac{\theta}{2}\right)\sin^2\left(\frac{\gamma}{2}\right)\nabla\phi_2 + \cos^2\left(\frac{\theta}{2}\right)\nabla\phi_s + 2e\mathbf{A}\right]^2 + \frac{\mathbf{B}^2}{2} + V_0 + V_{\rho Kn}.
\end{aligned} \tag{E9}$$

The variation of the second term in the free energy functional given in Eq. (E9) directly leads to the expression for the supercurrent:

$$\mathbf{J} = -4e\rho^2\left[\cos^2\left(\frac{\theta}{2}\right)\nabla\phi_s + \sin^2\left(\frac{\theta}{2}\right)\cos^2\left(\frac{\gamma}{2}\right)\nabla\phi_1 + \sin^2\left(\frac{\theta}{2}\right)\sin^2\left(\frac{\gamma}{2}\right)\nabla\phi_2 + 2e\mathbf{A}\right]. \tag{E10}$$

[1] C. Kallin and J. Berlinsky, Chiral superconductors, Rep. Prog. Phys. **79**, 054502 (2016).

[2] S. D. Sarma, M. Freedman, and C. Nayak, Majorana zero modes and topological quantum computation, npj Quantum Inf. **1**, 15001 (2015).

[3] M. Freedman, A. Kitaev, M. Larsen, and Z. Wang, Topological quantum computation, Bull. Amer. Math. Soc. **40**, 31 (2003).

[4] C. Nayak, S. H. Simon, A. Stern, M. Freedman, and S. D. Sarma, Non-Abelian anyons and topological quantum computation, Rev. Mod. Phys. **80**, 1083 (2008).

[5] V. Lahtinen and J. Pachos, A short introduction to topological quantum computation, SciPost Phys. **3**, 021 (2017).

[6] X.-L. Qi, T. L. Hughes, and S.-C. Zhang, Chiral topological superconductor from the quantum Hall state, Phys. Rev. B **82**, 184516 (2010).

[7] M. Sato and Y. Ando, Topological superconductors: A review, Rep. Prog. Phys. **80**, 076501 (2017).

[8] P. Zhang, K. Yaji, T. Hashimoto, Y. Ota, T. Kondo, K. Okazaki, Z. Wang, J. Wen, G. D. Gu, H. Ding, *et al.*, Observation of topological superconductivity on the surface of an iron-based superconductor, Science **360**, 182 (2018).

[9] S. M. Frolov, M. J. Manfra, and J. D. Sau, Topological superconductivity in hybrid devices, Nat. Phys. **16**, 718 (2020).

[10] Y. Tanaka, S. Tamura, and J. Cayao, Theory of Majorana zero modes in unconventional superconductors, Prog. Theor. Exp. Phys. **2024**, 08C105 (2024).

[11] R. M. Lutchyn, E. P. A. M. Bakkers, L. P. Kouwenhoven, P. Krogstrup, C. M. Marcus, and Y. Oreg, Majorana zero modes in superconductor–semiconductor heterostructures, Nat. Rev. Mater. **3**, 52 (2018).

[12] H.-H. Sun and J.-F. Jia, Detection of Majorana zero mode in the vortex, npj Quantum Mater. **2**, 34 (2017).

[13] K. Flensberg, F. von Oppen, and A. Stern, Engineered platforms for topological superconductivity and Majorana zero modes, Nat. Rev. Mater. **6**, 944 (2021).

[14] A. Mercado, S. Sahoo, and M. Franz, High-temperature Majorana zero modes, Phys. Rev. Lett. **128**, 137002 (2022).

[15] C. W. J. Beenakker, Search for Majorana fermions in superconductors, Annu. Rev. Condens. Matter Phys. **4**, 113 (2013).

[16] M. Sato and S. Fujimoto, Majorana fermions and topology in superconductors, J. Phys. Soc. Jpn. **85**, 072001 (2016).

[17] M. Franz, Race for Majorana fermions, Physics **3**, 24 (2010).

[18] A. Rahmani and M. Franz, Interacting Majorana fermions, Rep. Prog. Phys. **82**, 084501 (2019).

[19] A. Furusaki, M. Matsumoto, and M. Sigrist, Spontaneous Hall effect in a chiral p-wave superconductor, Phys. Rev. B **64**, 054514 (2001).

[20] T. Yokoyama, C. Iniotakis, Y. Tanaka, and M. Sigrist, Chirality sensitive effect on surface states in chiral p-wave superconductors, Phys. Rev. Lett. **100**, 177002 (2008).

[21] C. Kallin, Chiral p-wave order in Sr_2RuO_4, Rep. Prog. Phys. **75**, 042501 (2012).

[22] K. D. Nelson, Z. Q. Mao, Y. Maeno, and Y. Liu, Odd-parity superconductivity in Sr_2RuO_4, Science **306**, 1151 (2004).

[23] G. M. Luke, Y. Fudamoto, K. M. Kojima, M. I. Larkin, J. Merrin, B. Nachumi, Y. J. Uemura, Y. Maeno, Z. Q. Mao, Y. Mori, *et al.*, Time-reversal symmetry-breaking superconductivity in Sr_2RuO_4, Nature (London) **394**, 558 (1998).

[24] Y. Maeno, S. Kittaka, T. Nomura, S. Yonezawa, and K. Ishida, Evaluation of spin-triplet superconductivity in Sr_2RuO_4, J. Phys. Soc. Jpn. **81**, 011009 (2012).

[25] A. P. Mackenzie, T. Scaffidi, C. W. Hicks, and Y. Maeno, Even odder after twenty-three years: The superconducting order parameter puzzle of Sr_2RuO_4, npj Quantum Mater. **2**, 40 (2017).

[26] R. Fittipaldi, R. Hartmann, M. T. Mercaldo, S. Komori, A. Bjørlig, W. Kyung, Y. Yasui, T. Miyoshi, L. A. B. O. Olthof, C. M. P. Garcia, *et al.*, Unveiling unconventional magnetism at the surface of Sr_2RuO_4, Nat. Commun. **12**, 5792 (2021).

[27] T. Tummuru, O. Can, and M. Franz, Chiral p-wave superconductivity in a twisted array of proximitized quantum wires, Phys. Rev. B **103**, L100501 (2021).

[28] M. H. Fischer, T. Neupert, C. Platt, A. P. Schnyder, W. Hanke, J. Goryo, R. Thomale, and M. Sigrist, Chiral d-wave superconductivity in SrPtAs, Phys. Rev. B **89**, 020509 (2014).

[29] J.-F. Liu, Y. Xu, and J. Wang, Identifying the chiral d-wave superconductivity by Josephson ϕ_0-states, Sci. Rep. **7**, 43899 (2017).

[30] O. A. Awoga, A. Bouhon, and A. M. Black-Schaffer, Domain walls in a chiral d-wave superconductor on the honeycomb lattice, Phys. Rev. B **96**, 014521 (2017).

[31] S. Kittaka, Y. Shimizu, T. Sakakibara, Y. Haga, E. Yamamoto, Y. Ōnuki, Y. Tsutsumi, T. Nomoto, H. Ikeda, and K. Machida, Evidence for chiral d-wave superconductivity in URu_2Si_2 from the field-angle variation of its specific heat, J. Phys. Soc. Jpn. **85**, 033704 (2016).

[32] O. Can, T. Tummuru, R. P. Day, I. Elfimov, A. Damascelli, and M. Franz, High-temperature topological superconductivity in twisted double-layer copper oxides, Nat. Phys. **17**, 519 (2021).

[33] W.-S. Wang, Y.-C. Liu, Y.-Y. Xiang, and Q.-H. Wang, Antiferromagnetism, f-wave, and chiral p-wave superconductivity in a kagome lattice with possible application to sd^2 graphenes, Phys. Rev. B **94**, 014508 (2016).

[34] E. R. Schemm, W. J. Gannon, C. M. Wishne, W. P. Halperin, and A. Kapitulnik, Observation of broken time-reversal symmetry in the heavy-fermion superconductor UPt_3, Science **345**, 190 (2014).

[35] J. A. Sauls, The order parameter for the superconducting phases of UPt_3, Adv. Phys. **43**, 113 (1994).

[36] K. E. Avers, W. J. Gannon, S. J. Kuhn, W. P. Halperin, J. A. Sauls, L. DeBeer-Schmitt, C. D. Dewhurst, J. Gavilano, G. Nagy, U. Gasser, *et al.*, Broken time-reversal symmetry in the topological superconductor UPt_3, Nat. Phys. **16**, 531 (2020).

[37] J. D. Strand, D. J. Bahr, D. J. Van Harlingen, J. P. Davis, W. J. Gannon, and W. P. Halperin, The transition between real and complex superconducting order parameter phases in UPt_3, Science **328**, 1368 (2010).

[38] T. Ito, H. Takagi, S. Ishibashi, T. Ido, and S. Uchida, Normal-state conductivity between CuO_2 planes in copper oxide superconductors, Nature (London) **350**, 596 (1991).

[39] W. E. Pickett, Electronic structure of the high-temperature oxide superconductors, Rev. Mod. Phys. **61**, 433 (1989).

[40] J. M. Tranquada, H. Woo, T. G. Perring, H. Goka, G. D. Gu, G. Xu, M. Fujita, and K. Yamada, Quantum magnetic excitations from stripes in copper-oxide superconductors, Nature (London) **429**, 534 (2004).

[41] B. Keimer, S. A. Kivelson, M. R. Norman, S. Uchida, and J. Zaanen, From quantum matter to high-temperature superconductivity in copper oxides, Nature (London) **518**, 179 (2015).

[42] R. A. Klemm, Phenomenological model of the copper oxide superconductors, Phys. Rev. B **41**, 2073 (1990).

[43] P. M. R. Brydon, D. S. L. Abergel, D. F. Agterberg, and V. M. Yakovenko, Loop currents and anomalous Hall effect from time-reversal symmetry-breaking superconductivity on the honeycomb lattice, Phys. Rev. X **9**, 031025 (2019).

[44] W. Wu, M. M. Scherer, C. Honerkamp, and K. Le Hur, Correlated Dirac particles and superconductivity on the honeycomb lattice, Phys. Rev. B **87**, 094521 (2013).

[45] A. M. Black-Schaffer, W. Wu, and K. Le Hur, Chiral d-wave superconductivity on the honeycomb lattice close to the Mott state, Phys. Rev. B **90**, 054521 (2014).

[46] T. Ying and S. Yang, Superconducting pairing symmetries of the Hubbard model on the honeycomb lattice with inhomogeneous hopping strength, Phys. Rev. B **102**, 125125 (2020).

[47] B. Roy and I. F. Herbut, Unconventional superconductivity on honeycomb lattice: Theory of Kekule order parameter, Phys. Rev. B **82**, 035429 (2010).

[48] Y.-P. Lin and R. M. Nandkishore, Kohn-Luttinger superconductivity on two orbital honeycomb lattice, Phys. Rev. B **98**, 214521 (2018).

[49] S.-Q. Su, K. M. Tam, and H. Q. Lin, Evolution of superconductor pairing interactions from weak to strong coupling on a honeycomb lattice, Phys. Rev. B **80**, 104517 (2009).

[50] X. Y. Xu, S. Wessel, and Z. Y. Meng, Competing pairing channels in the doped honeycomb lattice Hubbard model, Phys. Rev. B **94**, 115105 (2016).

[51] E. Persky, A. Fang, X. Zhang, C. Adamo, E. Levenson-Falk, C. Shekhar, C. Felser, B. Yan, and A. Kapitulnik, "Possible unconventional surface superconductivity in the half-Heusler compound YPtBi, Phys. Rev. B **111**, 245417 (2025).

[52] T. Schwemmer, D. Di Sante, J. Schmalian, and R. Thomale, Chiral surface superconductivity in half-Heusler semimetals, arXiv:2212.09786.

[53] M. Yankowitz, S. Chen, H. Polshyn, Y. Zhang, K. Watanabe, T. Taniguchi, D. Graf, A. F. Young, and C. R. Dean, Tuning

superconductivity in twisted bilayer graphene, Science **363**, 1059 (2019).

[54] G. Tarnopolsky, A. J. Kruchkov, and A. Vishwanath, Origin of magic angles in twisted bilayer graphene, Phys. Rev. Lett. **122**, 106405 (2019).

[55] Y. Cao, D. Rodan-Legrain, O. Rubies-Bigorda, J. M. Park, K. Watanabe, T. Taniguchi, and P. Jarillo-Herrero, Tunable correlated states and spin-polarized phases in twisted bilayer–bilayer graphene, Nature (London) **583**, 215 (2020).

[56] S. Lisi, X. Lu, T. Benschop, T. A. de Jong, P. Stepanov, J. R. Duran, F. Margot, I. Cucchi, E. Cappelli, A. Hunter, *et al.*, Observation of flat bands in twisted bilayer graphene, Nat. Phys. **17**, 189 (2021).

[57] A. Kerelsky, L. J. McGilly, D. M. Kennes, L. Xian, M. Yankowitz, S. Chen, K. Watanabe, T. Taniguchi, J. Hone, C. Dean, *et al.*, Maximized electron interactions at the magic angle in twisted bilayer graphene, Nature (London) **572**, 95 (2019).

[58] P. Moon and M. Koshino, Optical absorption in twisted bilayer graphene, Phys. Rev. B **87**, 205404 (2013).

[59] R. Samajdar and M. S. Scheurer, Microscopic pairing mechanism, order parameter, and disorder sensitivity in moiré superlattices: Applications to twisted double-bilayer graphene, Phys. Rev. B **102**, 064501 (2020).

[60] T. J. Peltonen, R. Ojajärvi, and T. T. Heikkilä, Mean-field theory for superconductivity in twisted bilayer graphene, Phys. Rev. B **98**, 220504 (2018).

[61] Y. Cao, D. Rodan-Legrain, J. M. Park, N. F. Q. Yuan, K. Watanabe, T. Taniguchi, L. Fu, and P. Jarillo-Herrero, "Nematicity and competing orders in superconducting magic-angle graphene, Science **372**, 264 (2021).

[62] Y. Wang, J. Kang, and R. M. Fernandes, Topological and nematic superconductivity mediated by ferro-SU (4) fluctuations in twisted bilayer graphene, Phys. Rev. B **103**, 024506 (2021).

[63] O. Can, X.-X. Zhang, C. Kallin, and M. Franz, Probing time reversal symmetry breaking topological superconductivity in twisted double layer copper oxides with polar Kerr effect, Phys. Rev. Lett. **127**, 157001 (2021).

[64] Y. Yu, L. Ma, P. Cai, R. Zhong, C. Ye, J. Shen, G. D. Gu, X. H. Chen, and Y. Zhang, High-temperature superconductivity in monolayer $Bi_2Sr_2CaCu_2O_{8+\delta}$, Nature (London) **575**, 156 (2019).

[65] C. Xu, W. Yang, and C. Wu, Frustrated superconducting junction with tricomponent pairing gap functions, Phys. Rev. B **108**, 094509 (2023).

[66] G. M. Luke, A. Keren, L. P. Le, W. D. Wu, Y. J. Uemura, D. A. Bonn, L. Taillefer, and J. D. Garrett, Muon spin relaxation in UPt_3, Phys. Rev. Lett. **71**, 1466 (1993).

[67] Y. J. Uemura, T. Yamazaki, D. R. Harshman, M. Senba, and E. J. Ansaldo, Muon-spin relaxation in *Au*Fe and *Cu*Mn spin glasses, Phys. Rev. B **31**, 546 (1985).

[68] R. C. Jaklevic, J. Lambe, A. H. Silver, and J. E. Mercereau, Quantum interference effects in Josephson tunneling, Phys. Rev. Lett. **12**, 159 (1964).

[69] F. Giazotto and M. J. Martínez-Pérez, The Josephson heat interferometer, Nature (London) **492**, 401 (2012).

[70] D. Gerace, H. E. Türeci, A. Imamoglu, V. Giovannetti, and R. Fazio, The quantum-optical Josephson interferometer, Nat. Phys. **5**, 281 (2009).

[71] T. A. Fulton, L. N. Dunkleberger, and R. C. Dynes, Quantum interference properties of double Josephson junctions, Phys. Rev. B **6**, 855 (1972).

[72] C.-A. Li, J. Li, and S.-Q. Shen, Majorana-Josephson interferometer, Phys. Rev. B **99**, 100504 (2019).

[73] J. Song, H. Liu, J. Liu, Y.-X. Li, R. Joynt, Q.-F. Sun, and X. C. Xie, Quantum interference in topological insulator Josephson junctions, Phys. Rev. B **93**, 195302 (2016).

[74] A. Ferreira, J. Viana-Gomes, Y. V. Bludov, V. Pereira, N. M. R. Peres, and A. H. Castro Neto, Faraday effect in graphene enclosed in an optical cavity and the equation of motion method for the study of magneto-optical transport in solids, Phys. Rev. B **84**, 235410 (2011).

[75] L. R. Ingersoll, The kerr rotation for transverse magnetic fields, and the experimental verification of wind's magneto-optic theory, Phys. Rev. (Series I) **35**, 312 (1912).

[76] A. Cebollada, D. Weller, J. Sticht, G. R. Harp, R. F. C. Farrow, R. F. Marks, R. Savoy, and J. C. Scott, Enhanced magneto-optical Kerr effect in spontaneously ordered FePt alloys: Quantitative agreement between theory and experiment, Phys. Rev. B **50**, 3419 (1994).

[77] R. Shimano, G. Yumoto, J. Y. Yoo, R. Matsunaga, S.-I. Tanabe, H. Hibino, T. Morimoto, and H. Aoki, Quantum Faraday and Kerr rotations in graphene, Nat. Commun. **4**, 1841 (2013).

[78] H.-Ch. Mertins, S. Valencia, D. Abramsohn, A. Gaupp, W. Gudat, and P. M. Oppeneer, X-ray Kerr rotation and ellipticity spectra at the $2p$ edges of Fe, Co, and Ni, Phys. Rev. B **69**, 064407 (2004).

[79] R. R. Subkhangulov, R. V. Mikhaylovskiy, A. K. Zvezdin, V. V. Kruglyak, Th. Rasing, and A. V. Kimel, Terahertz modulation of the Faraday rotation by laser pulses via the optical Kerr effect, Nat. Photon. **10**, 111 (2016).

[80] W. K. Tse and A. H. MacDonald, Magneto-optical Faraday and Kerr effects in topological insulator films and in other layered quantized Hall systems, Phys. Rev. B **84**, 205327 (2011).

[81] Y. Marui, M. Kawaguchi, S. Sumi, T. Kikkawa, K. Sato, and M. Shiraishi, Spin and orbital Hall currents detected via current-induced magneto-optical Kerr effect in V and Pt, Phys. Rev. B **108**, 144436 (2023).

[82] E. Babaev, Vortices with fractional flux in two-gap superconductors and in extended Faddeev model, Phys. Rev. Lett. **89**, 067001 (2002).

[83] J. Garaud, J. Carlström, E. Babaev, and M. Speight, Chiral $\mathbb{C}P^2$ skyrmions in three-band superconductors, Phys. Rev. B **87**, 014507 (2013).

[84] T. A. Bojesen, E. Babaev, A. Sudbø, Time reversal symmetry breakdown in normal and superconducting states in frustrated three-band systems, Phys. Rev. B **88**, 220511 (2013).

[85] J. Garaud, J. Carlström, and E. Babaev, Topological solitons in three-band superconductors with broken time reversal symmetry, Phys. Rev. Lett. **107**, 197001 (2011).

[86] J. Cao and S.-J. Xiong, Topological phase transition in a graphene system with a coexistence of Coulomb interaction, staggered potential, and intrinsic spin-orbit coupling, Phys. Rev. B **88**, 085409 (2013).

[87] Y. Hadad, A. B. Khanikaev, and A. Alù, Self-induced topological transitions and edge states supported by nonlinear staggered potentials, Phys. Rev. B **93**, 155112 (2016).

[88] R. Qi, J. Cao, and X.-P. Jiang, Multiple localization transitions and novel quantum phases induced by a staggered on-site potential, Phys. Rev. B **107**, 224201 (2023).
[89] D. J. Thouless, M. Kohmoto, P. Nightingale, and M. den Nijs, Quantized Hall conductance in a two-dimensional periodic potential, Phys. Rev. Lett. **49**, 405 (1982).
[90] B. Simons, Holonomy, the quantum Adiabatic theorem, and Berry's phase, Phys. Rev. Lett. **51**, 2167 (1983).
[91] T. Fukui, Y. Hatsugai, and H. Suzuki, Chern numbers in discretized Brillouin zone: Efficient method of computing (spin) Hall conductances, J. Phys. Soc. Jpn. **74**, 1674 (2005).
[92] K. Kudo, H. Watanabe, T. Kariyado, and Y. Hatsugai, Many-body Chern number without integration, Phys. Rev. Lett. **122**, 146601 (2019).
[93] P. Delplace, D. Ullmo, and G. Montambaux, Zak phase and the existence of edge states in graphene, Phys. Rev. B **84**, 195452 (2011).
[94] D. Obana, F. Liu, and K. Wakabayashi, Topological edge states in the Su-Schrieffer-Heeger model, Phys. Rev. B **100**, 075437 (2019).
[95] Y. Plotnik, M. C. Rechtsman, D. Song, M. Heinrich, J. M. Zeuner, S. Nolte, Y. Lumer, N. Malkova, J. Xu, A. Szameit, *et al.*, Observation of unconventional edge states in 'photonic graphene', Nat. Mater. **13**, 57 (2014).
[96] A. H. MacDonald, Edge states in the fractional-quantum-Hall-effect regime, Phys. Rev. Lett. **64**, 220 (1990).
[97] Y. Hatsugai, Chern number and edge states in the integer quantum Hall effect, Phys. Rev. Lett. **71**, 3697 (1993).
[98] P. N. Argyres, Theory of the Faraday and Kerr effects in ferromagnetics, Phys. Rev. **97**, 334 (1955).
[99] C. Brée, A. Demircan, and G. Steinmeyer, Saturation of the all-optical Kerr effect, Phys. Rev. Lett. **106**, 183902 (2011).
[100] K. N. Okada, Y. Takahashi, M. Mogi, R. Yoshimi, A. Tsukazaki, K. S. Takahashi, N. Ogawa, M. Kawasaki, and Y. Tokura, Terahertz spectroscopy on Faraday and Kerr rotations in a quantum anomalous Hall state, Nat. Commun. **7**, 12245 (2016).
[101] D. G. Ovalle, A. Pezo, and A. Manchon, Orbital Kerr effect and terahertz detection via the nonlinear Hall effect, Phys. Rev. B **110**, 094439 (2024).
[102] Z.-A. Hu, H.-W. Wang, B. Fu, J.-Y. Zou, and S.-Q. Shen, Signature of parity anomaly in the measurement of optical Hall conductivity in quantum anomalous Hall systems, Phys. Rev. B **106**, 035149 (2022).
[103] J. M. Parent, R. Côté, and I. Garate, Magneto-optical Kerr effect and signature of the chiral anomaly in a Weyl semimetal in magnetic field, Phys. Rev. B **102**, 245126 (2020).
[104] E. Taylor and C. Kallin, Intrinsic Hall effect in a multiband chiral superconductor in the absence of an external magnetic field, Phys. Rev. Lett. **108**, 157001 (2012).
[105] J. Goryo, Impurity-induced polar Kerr effect in a chiral *p*-wave superconductor, Phys. Rev. B **78**, 060501 (2008).